

# A volume-of-fluid method for simulation of compressible axisymmetric multi-material flow

D. de Niem<sup>a,\*</sup>, E. Kührt<sup>a</sup>, U. Motschmann<sup>a,b</sup>

<sup>a</sup> *Institute of Planetary Research, German Aerospace Center, Rutherford Str. 2, D-12489 Berlin, Germany*

<sup>b</sup> *Institute of Theoretical Physics, Technical University of Braunschweig, Mendelssohnstr. 3, D-38106 Braunschweig, Germany*

Received 1 May 2006; received in revised form 24 July 2006; accepted 13 September 2006

Available online 7 November 2006

## Abstract

A two-dimensional Eulerian hydrodynamic method for the numerical simulation of inviscid compressible axisymmetric multi-material flow in external force fields for the situation of pure fluids separated by macroscopic interfaces is presented. The method combines an implicit Lagrangian step with an explicit Eulerian advection step. Individual materials obey separate energy equations, fulfill general equations of state, and may possess different temperatures. Material volume is tracked using a piecewise linear volume-of-fluid method. An overshoot-free logically simple and economic material advection algorithm for cylinder coordinates is derived, in an algebraic formulation. New aspects arising in the case of more than two materials such as the material ordering strategy during transport are presented. One- and two-dimensional numerical examples are given.

© 2006 Elsevier B.V. All rights reserved.

PACS: 02.60.Cb; 47.11+j; 47.40.Nm; 62.50.+p

Keywords: Multi-material flow; Shock waves; Volume-of-fluid; Interface tracking; Cylindrical coordinates

## 1. Introduction

The simulation of multi-material hydrodynamic problems with moving boundaries is a challenge that led to the development of many algorithms including finite elements, gridless and grid-based Lagrangian and Eulerian finite difference methods, see [1] for a review. It is concerned with a common situation in nature: fluids have surfaces and boundaries, and although our understanding about fluid flow inside fixed boundaries has reached a great deal of sophistication, there is more complexity if we look towards the situation near a fluid surface. An illustrative example is the impact of a compressible solid object into water. In this work, the term multi-material flow is used in contrast to multi-phase or multi-fluid flow with the understanding that it describes a situation where several pure materials (i.e. fluids, solids and gases) are separated by *macroscopic* boundaries, called material interfaces, and a single velocity field ex-

ists that is common to all materials in a multi-material cell. In contrast, so-called multi-phase or multi-fluid flow, see [26–30], e.g., describes a situation where fluids may be thoroughly locally mixed and may also possess different velocities; momentum exchange terms between material species occur. Such models converge to a single velocity field in the limit of infinitely fast momentum relaxation [25,30].

Lagrangian multi-material methods seem to be best adapted to an arbitrary geometry of material boundaries, but severe resolution problems arise when large distortions or topological changes occur. This forces a frequent rezone operation, which leads to loss of information and accuracy, or technically demanding procedures preventing interpenetration if there is a separate grid associated with each material. Eulerian formulations using the volume-of-fluid (see Rider and Kothe [2], Gueyffier et al. [3] or Benson [5], for an overview) or the level set methods [6] can describe arbitrarily complex topology of material boundaries. Eulerian volume-of-fluid (VOF) methods with artificial viscosity for the treatment of shock waves have been developed over the past, e.g., CTH [10] or SOVA [11,12].

\* Corresponding author. Tel.: +49 30 67055 316; fax: +49 30 67055 386.  
E-mail address: [detlef.deniem@dlr.de](mailto:detlef.deniem@dlr.de) (D. de Niem).

Although Godunov-type methods are state of the art in the treatment of shocks and contact discontinuities for one-material conservative problems, there are few publications in combination with the VOF method, e.g., Miller and Puckett [7] or Miller and Colella [8]. Godunov-type methods have also been developed for the single-velocity limit of multi-fluid flow, e.g., [26–30], and there are claims that such algorithms work equally well for both situations, i.e. well-separated pure fluids and mixtures. However, these methods do not attempt to reconstruct the geometrical location of the material interface in the cell and their preferred application is the description of physics where actual mixtures of several materials respond to shock loading. The treatment of material interfaces between well-separated pure fluids by [26–30] is diffusive, and the change of the volume fraction is spread over more than ten cells in a typical example. This leads to broad zones with mixed fluid properties in the course of time, and the diffusion is irreversible.

An obstacle for a multi-material generalization of Godunov's method using the VOF approach is the presence of arbitrarily-directed explicit material boundaries in a computational cell, a geometry where no exact solution of a Riemann problem at the boundary between two cells is available. The only example so far combining a Godunov scheme with the VOF method [7], assumes a rather special form for the equation of state (EOS) and solves an effective one-material Riemann problem smearing the materials out uniformly in the two cells under consideration. This leads to fluxes of conserved quantities arising from the Riemann solver that are incompatible with the geometrically constructed advection terms for volume fraction. The discrete update of volume fraction is not overshoot-free, and subsequent truncation leads to an error in volume that is compensated by one in density. Another serious problem in multi-material Godunov-type methods is the treatment of geometric source terms caused by curvilinear coordinates or external forces. Consequently, [7] use Cartesian coordinates only. Problems arise in a near-hydrostatic or stationary situation in a gravity field, for example. There are suggestions to improve the situation in this case [9], however a multi-material generalization has not been published. More traditional VOF-based methods with artificial viscosity for the treatment of shock waves (see [10–12]) cope most naturally with geometrical source terms and additional forces.

In this work we present a Eulerian volume-of-fluid method for compressible multi-material flow with *macroscopic* interfaces between fluids. The algorithm uses a spatially staggered discretization in cylindrical coordinates and artificial viscosity for the treatment of shocks. The implementation in curvilinear coordinates is not at all straightforward and requires additional considerations in the VOF method; it leads to modifications in the advection scheme for momentum on a staggered mesh as well. These modifications and the explicit description of how to implement the VOF method have been omitted by previous works like [10] or [11,12] motivating a more comprehensive presentation of such aspects, here. Moreover, we derive a fully algebraic formulation of an overshoot-free piecewise linear VOF advection scheme in cylindrical coordinates. The treatment of pressure during the Lagrangian step is implicit, at

the cost to invert a tri-diagonal matrix for each one-dimensional row. We also present new aspects arising in the context of VOF methods when more than two materials share a multi-material cell, where the interface reconstruction and advection steps require a material ordering such that no intersections of different interface lines occur in a cell. A solution of this problem is developed in the case of three materials. Two-dimensional test problems for advection with three materials are presented in Section 5.1. Numerical examples in one dimension are compared to exact solutions and demonstrate the ability to correctly approximate shocks and rarefaction waves for simple and more difficult EOS. Further a two-dimensional axisymmetric example illustrates the full capabilities of the algorithm.

## 2. Governing equations

One of the basic assumptions in multi-material hydrodynamics is the existence of a velocity field common to all materials, and the Euler equation for inviscid axisymmetric flow is

$$\frac{\partial u^j}{\partial t} + u^i \frac{\partial u^j}{\partial x^i} = -\frac{1}{\rho} \frac{\partial p}{\partial x^j} + g^j, \quad (1)$$

where  $x^j = (r, z)$  are cylinder coordinates,  $u^j = (u, v)$  is the velocity,  $\rho$  and  $p$  are the total mass density and pressure, respectively, and  $g^j$  denotes the acceleration due to an external force. Because we restrict the algorithm to irrotational flow there is no azimuthal velocity component. Each material  $m$  is characterized by a volume fraction  $f^m \in \{0; 1\}$  normalized by  $\sum_m f^m = 1$  and mass density  $\rho^m$ . Conservation of mass of material  $m$  is expressed as (no sum over repeated material superscripts  $m$ )

$$\frac{\partial(r f^m \rho^m)}{\partial t} + \frac{\partial(r f^m \rho^m u^i)}{\partial x^i} = 0. \quad (2)$$

The continuity equation for the total density  $\rho := \sum_m f^m \rho^m$  results, when (2) is summed over species. Following [7], we assume that the internal energy  $\epsilon^m$  of each material evolves locally adiabatic

$$\frac{\partial \epsilon^m}{\partial t} + u^i \frac{\partial \epsilon^m}{\partial x^i} = \frac{p^m}{(\rho^m)^2} \left( \frac{\partial \rho^m}{\partial t} + u^i \frac{\partial \rho^m}{\partial x^i} \right), \quad (3)$$

here  $p^m$  is evaluated, using the equation of state of species  $m$ . The need for  $m$  separate energy equations arises in the absence of thermal equilibrium, i.e. unequal temperatures of materials. This is common in situations characterized by strong shocks in condensed media, in particular for impact-type problems, see [7], where the time to reach thermal equilibrium between materials in a computational cell can be much longer than the time scale of wave propagation through the cell. One more equation is necessary to close the system that takes the form ([7], see also [30]) in the general case

$$\frac{\partial f^m}{\partial t} + u^i \frac{\partial f^m}{\partial x^i} = f^m (\kappa^m - 1) \left( \frac{1}{r} \frac{\partial(r u^i)}{\partial x^i} \right), \quad (4)$$

where  $\kappa^m$  is a phenomenological parameter that depends on the physical model. It has to fulfill a normalization condition

$\sum_m f^m \kappa^m = 1$  that follows by summing Eq. (4) over  $m$ . Mixture theory as defined in [7] is obtained with

$$\kappa^m = \frac{\rho c^2}{\rho^m (c^m)^2}, \quad (5)$$

where  $c^m$  denotes the adiabatic sound speed of material  $m$ . Multiplying Eq. (5) by  $f^m$  and summing over species the bulk sound speed  $c$  in mixture theory is given by

$$\frac{1}{\rho c^2} = \sum_m \frac{f^m}{\rho^m (c^m)^2}. \quad (6)$$

This addition rule corresponds to a physical situation where materials are thoroughly mixed, like in a powder, and is not necessarily valid in a transition region where they are well separated by macroscopic interfaces. Miller and Puckett [7], who are assuming local pressure equilibrium among materials, proceed from the continuity equation (2) and relate the change of  $\rho^m$  along a flow line to that of the total density  $\rho$  with the help of the equation for the isentropic change of pressure to derive Eq. (4). Finally, they replace the change of the bulk density in terms of the velocity divergence, leading to Eq. (5).

If we do not assume local pressure equilibrium among species it is possible to show that conservation of total energy determines the rule to calculate the total pressure. From the Euler equation (1), the continuity equations (2) and the energy equations (3) one obtains (setting  $g^i = 0$ , for the moment)

$$\begin{aligned} \frac{\partial(f^m E^m)}{\partial t} + \frac{\partial(r f^m E^m u^i)}{r \partial x^i} \\ = -p^m \left( \frac{\partial f^m}{\partial t} + \frac{\partial(r f^m u^i)}{r \partial x^i} \right) - \left( \frac{f^m \rho^m}{\rho} \right) u^i \frac{\partial p}{\partial x^i}, \end{aligned} \quad (7)$$

where  $E^m = \rho^m (u^i u_i / 2 + \epsilon^m)$  is the total energy density of material  $m$ . Using Eq. (4) and summing over materials the usual conservative form of the inviscid energy equation is obtained, if the following condition holds

$$p = \sum_m f^m \kappa^m p^m. \quad (8)$$

The present formulation contains the case  $\forall m: \kappa_m = 1$  leading to the so-called color advection where Eq. (4) is the ordinary advection equation for a scalar quantity. It describes the transport of a material property that does not change as the material is compressed or expanded, in other words, the color of the species remains the same. The constraint of local pressure equilibrium, if fulfilled at the beginning, is destroyed by any numerical algorithm and has to be re-enforced after each time step by adiabatic relaxation in every multi-material cell (requiring multiple evaluations of the EOS). Local pressure equilibrium in multi-material cells is one of the most problematic issues leading to pressure oscillations and other phenomena, see [27] e.g. It is clear that equilibration of pressure in a computational cell cannot take place in a time shorter than that required for an acoustic wave to propagate through the entire cell, but numerical time steps are shorter than this, in general. On the other hand, in a true mixture containing microscopic inclusions—e.g., bubbles—of a second material, pressure equilibration by wave propagation over the distance of the bubble

diameter takes much less time; in this situation pressure equilibrium makes sense. Present versions of CTH [10] offer several alternative possibilities treating multi-material cells including differing pressures and temperatures of materials, etc. The view of the authors is that the simplest approach for materials in a computational cell with not too unequal compressibilities is to use color advection  $\forall m: \kappa^m = 1$ , and permit unequal pressures of materials together with the definition  $p = \sum_m f^m p^m$  following from Eq. (8). The composition law for the bulk sound speed then follows from

$$\frac{d}{dt} \sum_m f^m p^m = \sum_m f^m \frac{dp^m}{dt} = - \sum_m f^m \rho^m (c^m)^2 \nabla \cdot \vec{u}, \quad (9)$$

where  $d/dt$  denotes the convective derivative. The right-hand side follows from  $df^m/dt = 0$ , the isentropic pressure evolution of single materials,

$$\frac{dp^m}{dt} = (c^m)^2 \frac{d\rho^m}{dt}, \quad (10)$$

and the continuity equation (2). So the composition law for the bulk sound speed in the case of color advection  $\forall m: \kappa^m = 1$  is

$$\rho c^2 = \sum_m f^m \rho^m (c^m)^2. \quad (11)$$

We will only describe an algorithm for this case, here. Such a choice is more robust in difficult situations. Moreover, one-dimensional numerical examples demonstrate that this does not produce oscillations of bulk pressure or velocity across material interfaces and that physical wave speeds in shock tube and impact-type problems are well approximated. This holds for problems where multi-material zones are narrow transition regions and the flow is of a single-material character elsewhere.

### 3. Numerical scheme

#### 3.1. Staggered spatial grid formulation

Our numerical method is a fixed-grid Eulerian approach using a Lagrange-plus-Remap strategy. It is logically more simple for multi-material problems to subdivide the algorithm into a Lagrangian step, where mass is conserved and the computational grid is moving, followed by an Eulerian advection step, where mass, momentum and energy in the overlapping part of the grid resulting after the Lagrangian step are re-distributed conservatively onto the original Eulerian grid, see [1,10] e.g. We use a spatially staggered grid: densities, volume fractions and internal energies are cell-centred, whereas the velocity components reside at the midpoint of the cell edges, see Fig. 1. To fix the notation cell-centred state variables bear half-integer indices; cell  $(i + 1/2, j + 1/2)$  is the region  $\{r_i; r_{i+1}\} \times \{z_j; z_{j+1}\}$ . The radial velocity  $u_{i,j+1/2}$  is attached to the midpoint of the left cell edge  $r_{i,j+1/2}$ , likewise the  $z$ -velocity  $v_{i+1/2,j}$  to the midpoint of the lower edge  $z_{i+1/2,j}$ . All variables belong to the same time level. This is mentioned because there are schemes where the velocities are staggered in time as well [10]. In the following, we start with an algorithm overview, than we describe the part of the Lagrangian and Eulerian (remap) steps that can be understood

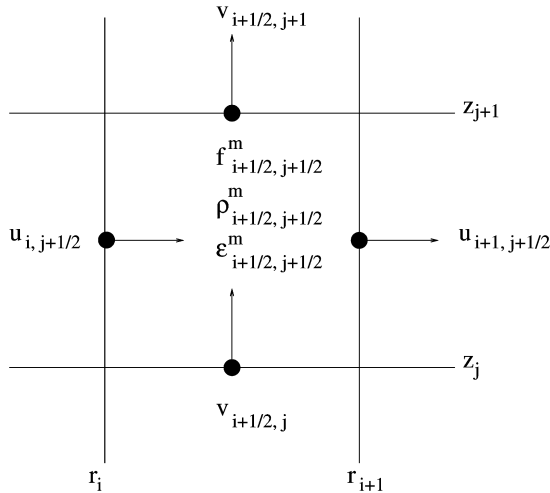


Fig. 1. Staggered mesh discretization, position of variables.

without special consideration of the material advection algorithm. A subsequent section describes the implementation of the volume-of-fluid method.

### 3.2. Algorithm overview

The multi-dimensional algorithm uses operator splitting. The two operators are analogous; it suffices to describe the part for the radial direction more comprehensively.

For each direction, the beginning operation is always a VOF interface reconstruction on the whole two-dimensional mesh. At boundaries constant extrapolation of volume fraction is used. This procedure is two-dimensional but all remaining steps are of a one-dimensional nature. A non-intersecting construction of material interfaces—the onion skin partition—is applied in cells with more than two materials. Additionally, the area subtended by each material in the  $r$ - $z$  plane has to be found in multi-material cells with the help of the interface geometry; this is only required for the radial direction. The initial state vector at time  $t_n$  consists of the cell-centred volume fractions, mass densities and internal energies ( $f_{i+1/2,j+1/2}^m$ ,  $\rho_{i+1/2,j+1/2}^m$ ,  $\epsilon_{i+1/2,j+1/2}^m$ ) and of the velocities ( $u_{i,j+1/2}$ ,  $v_{i+1/2,j}$ ) associated with the edges of the cell.

The one-dimensional Lagrangian step is a leapfrog scheme where new radial velocities  $\tilde{u}_{i,j+1/2}$  arise due to the acceleration by pressure gradient and external forces evaluated at a half time step. This leads to a time-implicit algorithm. For each material occupying a computational cell in the one-dimensional row in radial direction, the EOS is evaluated and pressures as well as sound speeds are obtained; the artificial viscosity term is added to the pressure. These pressures and sound speeds at  $t_n$  are sufficient to approximate pressure at half time steps, leading to a tri-diagonal system (linearization is inherent in the approximation of time-centred pressure), which is solved to obtain radial velocities at  $t_{n+1}$ . No changes occur for the transverse velocity components  $v_{i+1/2,j}$ . Mass is conserved, so it is not required to update densities. The coefficients of the tri-diagonal system only contain total pressures and sound speeds, formed as suitable averages over materials in a cell. Knowing the new

radial velocities the approximate pressures at half time steps,  $P_{i+1/2,j+1/2}^{m,1/2}$ , are determined. The latter are used to compute the new internal energies, so at the end of the Lagrangian step we know  $(\tilde{u}_{i,j+1/2}, \tilde{\epsilon}_{i+1/2,j+1/2}^m)$ . The change of the geometry of material interfaces is considered later as part of the Eulerian pseudo-flux calculation for material volume.

In the Eulerian or remap step we evaluate the effect of the overlap between the original Eulerian and new Lagrangian grids. The remap step is based on a linear redistribution of material volume, mass, energy and momentum using the advective flux of volume and mass of individual materials. Knowing the time-averaged velocities  $u_i^*$  and the geometry of the interface there is enough information to obtain the Eulerian remap fluxes across edges  $r_i$  for the cell-centred quantities. The auxiliary quantities to be calculated are the advected volumes  $V_i^{m,(adv)}$  and transport masses  $M_i^{m,(adv)}$ . The transport mass (defining the mass flux) uses characteristic traceback and hence only needs the original density at  $t_n$  in the donor cell, see the subsection on advected masses. For volume fraction, there appear more complicated pseudo-fluxes that include the modification of geometry due to the Lagrangian step, see the section on the volume-of-fluid method. The remap flux for cell-centred internal energies is based on the mass flux and the  $\tilde{\epsilon}_{i+1/2,j+1/2}^m$  in the donor (upwind) cell. Because momentum is defined with respect to a different grid we then form mass fluxes with respect to the “dual” grid, as described in the subsection on momentum advection. These fluxes are also necessary to update the nodal masses. This incorporates different rules for the longitudinal and transverse momentum, in particular, the mass flux for the control volume associated with  $v_{i+1/2,j}$  has to use mass fluxes in radial direction for two vertically adjacent cells, requiring modest additional storage. Thereafter we construct the momentum flux based on a monotized upwind-biased linear interpolation of velocity after the Lagrangian step. Nodal masses have to be updated along with momentum resulting in new Eulerian velocities. Finally, a modified state vector at  $t_{n+1}$  valid on the Eulerian grid is obtained. It contains only the modification due to the operator-split part of the algorithm in the radial direction. It serves as input for the operator to follow in  $z$ -direction. This completes the execution of the one-dimensional flow solver at the current layer; the succession of one-dimensional procedures is repeated until the last layer in  $z$ -direction is reached.

Then, the material interfaces are reconstructed again on the fixed Eulerian grid. Now the succession of one-dimensional Lagrangian steps followed by Eulerian remap is repeated for the rows in  $z$ -direction. This time,  $v_{i+1/2,j}$  gets modified during the Lagrangian step, and the role of longitudinal and transverse momentum is exchanged. To avoid aliasing effects the sequence of operator-split steps in the radial and  $z$ -direction is alternated during subsequent time steps. The details of the numerical algorithm are described in the following.

### 3.3. Lagrangian step

#### 3.3.1. Radial direction

In this work, dimensional splitting is required due to an implicit method to estimate pressure in the discretization of

Euler's equation, adopted from [11]. Due to operator splitting, the Lagrangian step can be described in a one-dimensional framework. The radial direction is more complicated, therefore we describe it in some more detail. During a time interval  $\Delta t$  the edges  $r_i$  of the cells in radial direction are thought to move as

$$\tilde{r}_i = r_i + u_i^* \Delta t, \quad u_i^* := \frac{1}{2}(u_i + \tilde{u}_i), \quad (12)$$

where  $u_i^*$  is the time-average of radial velocity, in terms of  $u_i$  and  $\tilde{u}_i$ , the values at the beginning and end of the Lagrangian step, respectively. A common half-integer index  $j + 1/2$  for the layer in the  $z$ -direction will be omitted to simplify notation. The radial part of the Euler equation is not in conservation form for momentum. Following the ideas in [13] its discrete version is written as

$$\tilde{u}_i = u_i - \frac{(p_{i+1/2}^{1/2} - p_{i-1/2}^{1/2})\Delta t}{[\rho_{i+1/2}(r_{i+1/2} - r_i) + \rho_{i-1/2}(r_i - r_{i-1/2})]} + g_{r,i}\Delta t, \quad (13)$$

where  $r_{i+1/2}$  denote the radial coordinates of the cell centre,  $p_{i+1/2}^{1/2}$  is an approximation for the pressure after a half time step, and  $g_{r,i}$  is the radial acceleration due to an external force acting at  $r_i$ . The total densities in the denominator are volume-fraction averages of cell-centred values

$$\rho_{i+1/2} = \sum_m f_{i+1/2}^m \rho_{i+1/2}^m. \quad (14)$$

Note that Eq. (13) fulfills the consistency condition that for a radially constant pressure profile no acceleration is generated in the absence of external forces.<sup>1</sup> The approximation for  $p_{i+1/2}^{1/2}$  is implicit in terms of the velocities  $\tilde{u}_i$  and results from the discrete form of the equation for the change of total pressure along a Lagrangian trajectory (9)

$$p_{i+1/2}^{1/2} = p_{i+1/2} + q_{i+1/2} - \rho_{i+1/2}(c_{i+1/2})^2 \times \left( \frac{r_{i+1}\tilde{u}_{i+1} - r_i\tilde{u}_i}{r_{i+1/2}(r_{i+1} - r_i)} \right) \frac{\Delta t}{2}, \quad (15)$$

where  $p_{i+1/2}$  is evaluated with the help of the pressure addition law (8). The bulk sound speed  $c_{i+1/2}$  is evaluated with the help of Eq. (24) below. Further,  $q_{i+1/2}$  is a quadratic Von Neumann and Richtmeyer artificial viscosity formed with the help of velocity and density at the begin of the Lagrangian step. The numerical approximation of the velocity divergence in the right-hand side of Eq. (15) is motivated by the fact that any higher-order terms containing velocity squares would render the tri-diagonal system (16) non-linear in velocities. One now eliminates  $p_{i\pm 1/2}^{1/2}$  in Eq. (13) with the help of Eq. (15), and a tri-diagonal linear system of equations is obtained for the  $\tilde{u}_i$

$$-A_i\tilde{u}_{i+1} + B_i\tilde{u}_i - C_i\tilde{u}_{i-1} = D_i, \quad (16)$$

where the coefficients are given by

$$A_i = \frac{\rho_{i+1/2}(c_{i+1/2}\Delta t)^2}{2(\rho\Delta r)_i} \frac{r_{i+1}}{r_{i+1/2}(r_{i+1} - r_i)}, \quad (17)$$

$$C_i = \frac{\rho_{i-1/2}(c_{i-1/2}\Delta t)^2}{2(\rho\Delta r)_i} \frac{r_{i-1}}{r_{i-1/2}(r_i - r_{i-1})}, \quad (18)$$

$$D_i = u_i - \frac{\Delta t}{(\rho\Delta r)_i} [(p+q)_{i+1/2} - (p+q)_{i-1/2}] + g_{r,i}\Delta t, \quad (19)$$

$$B_i = 1 + \frac{\rho_{i+1/2}(c_{i+1/2}\Delta t)^2}{2(\rho\Delta r)_i} \frac{r_i}{r_{i+1/2}(r_{i+1} - r_i)} + \frac{\rho_{i-1/2}(c_{i-1/2}\Delta t)^2}{2(\rho\Delta r)_i} \frac{r_i}{r_{i-1/2}(r_i - r_{i-1})}, \quad (20)$$

with the abbreviation

$$(\rho\Delta r)_i := \rho_{i+1/2}(r_{i+1/2} - r_i) + \rho_{i-1/2}(r_i - r_{i-1/2}). \quad (21)$$

All quantities occurring in the coefficients  $A_i \dots D_i$  belong to the initial time level. The system of Eqs. (16) is solved with the so-called double sweep method, see [13,14], taking boundary conditions into account (at boundaries, we replace (16) by first-order differential relations connecting values at two nodes only [14], see [16] for non-reflecting boundary conditions). After the velocities  $\tilde{u}_i$  have been found, the effect of the Lagrangian step on other state variables can be obtained. The energy equations (3) are discretized as

$$\tilde{\epsilon}_{i+1/2}^m = \epsilon_{i+1/2}^m - \frac{p_{i+1/2}^{m,1/2}}{\rho_{i+1/2}^m} \frac{(r_{i+1}u_{i+1}^* - r_i u_i^*)}{r_{i+1/2}(r_{i+1} - r_i)} \Delta t, \quad (22)$$

where we used the continuity equations (2) and color advection to arrive at this particularly simple form. The discrete approximation of the velocity divergence in (22) is justified by total energy conservation during the Lagrangian step, see Appendix A for details. The following expression for the half time step pressure of species  $m$  is a discrete approximation of Eq. (10)

$$p_{i+1/2}^{m,1/2} = p_{i+1/2}^m + q_{i+1/2}^m - \rho_{i+1/2}^m (c_{i+1/2}^m)^2 \frac{(r_{i+1}\tilde{u}_{i+1} - r_i\tilde{u}_i)}{r_{i+1/2}(r_{i+1} - r_i)} \frac{\Delta t}{2}, \quad (23)$$

and it can be verified that by multiplying this equation with  $f_{i+1/2}^m$  and summing over materials, one obtains Eq. (15) for the half time step value of the bulk pressure, if the definition of the bulk sound speed is

$$\rho_{i+1/2} c_{i+1/2}^2 = \sum_m f_{i+1/2}^m \rho_{i+1/2}^m (c_{i+1/2}^m)^2. \quad (24)$$

By virtue of Eq. (23) the artificial viscosity is present in the work term for internal energy, Eq. (22).

### 3.3.2. $z$ -direction

Most equations for the radial part of the dimensionally split algorithm are valid for the  $z$ -direction as well with only minor change. The discrete version of Euler's equation (13) is obtained by the substitution  $u_i \rightarrow v_j$ ,  $r_i \rightarrow z_j$ ,  $r_{i+1/2} \rightarrow z_{j+1/2}$  and  $g_{r,i} \rightarrow g_{z,j}$  (again we suppress a half-integer index  $i + 1/2$  common to all variables). The tri-diagonal system obtained for the  $z$  velocity is analogous to Eq. (16) with the substitution

<sup>1</sup> This also requires vanishing of the discrete velocity divergence.



$\tilde{u}_i \rightarrow \tilde{v}_j$ . The coefficients are given by

$$A_j = \frac{\rho_{j+1/2}(c_{j+1/2}\Delta t)^2}{2(\rho\Delta z)_j(z_{j+1} - z_j)}, \quad (25)$$

$$C_j = \frac{\rho_{j-1/2}(c_{j-1/2}\Delta t)^2}{2(\rho\Delta z)_j(z_j - z_{j-1/2})}, \quad (26)$$

$$D_j = v_j - \frac{\Delta t}{(\rho\Delta z)_j}[(p+q)_{j+1/2} - (p+q)_{j-1/2}] + g_{z,j}\Delta t, \quad (27)$$

$$B_j = 1 + A_j + C_j, \quad (28)$$

where  $(\rho\Delta z)_j$  is the abbreviation

$$(\rho\Delta z)_j = \rho_{j+1/2}(z_{j+1/2} - z_j) + \rho_{j-1/2}(z_j - z_{j-1/2}). \quad (29)$$

The update of internal energy during the Lagrangian step analogous to Eq. (22) is given by

$$\tilde{\epsilon}_{j+1/2}^m = \epsilon_{j+1/2}^m - \frac{p_{j+1/2}^{m,1/2}}{\rho_{j+1/2}^m} \left( \frac{v_{j+1}^* - v_j^*}{z_{j+1} - z_j} \right) \Delta t, \quad (30)$$

where the half time step pressure is obtained from

$$p_{j+1/2}^{m,1/2} = p_{j+1/2}^m + q_{j+1/2}^m - \rho_{j+1/2}^m (c_{j+1/2}^m)^2 \left( \frac{\tilde{v}_{j+1} - \tilde{v}_j}{z_{j+1} - z_j} \right) \frac{\Delta t}{2}, \quad (31)$$

and  $v_j^*$  is a time-averaged  $z$  velocity in analogy to Eq. (12).

The expression for the total pressure  $p_{j+1/2}^{1/2}$  in terms of individual pressures as well as the addition rule for the squared sound speed are the same as before.

### 3.4. Eulerian remap step

#### 3.4.1. Discrete continuity equations

The Lagrangian step conserves the mass of each material, so only the advected mass contained in the overlap region in between the Eulerian and Lagrangian grid positions,  $r_i$  and  $r_i + u_i^* \Delta t$ , has to be found (see Fig. 3 for the radial direction). The numerical mass flux of material  $m$  through edge  $i$  is defined as

$$\Phi_i^m = \frac{M_i^{m,(\text{adv})}}{\Delta z \Delta t}, \quad (32)$$

where  $M_i^{m,(\text{adv})}$  denotes the advected mass of species  $m$ . It has the same sign as the velocity  $u_i^*$ . This quantity is evaluated with the help of the volume-of-fluid method, see Section 4.5, for more detail. The discretization of the continuity equation for species  $m$ , Eq. (2) during the remap step in  $r$ -direction then takes the following form

$$(f^m \rho^m)_{i+1/2}^{n+1} = (f^m \rho^m)_{i+1/2}^n - \frac{\Delta t}{r_{i+1/2}(r_{i+1} - r_i)} (\Phi_{i+1}^m - \Phi_i^m), \quad (33)$$

where the superscripts  $n$  and  $n+1$  denote subsequent time levels. The last equation is the full discretization of the radial part of the continuity equations in Eulerian finite volume form. The expressions for the substep in  $z$ -direction are similar and not given here.

#### 3.4.2. Eulerian finite volume update of internal energy

To derive a consistent discretization of the equation for the internal energy one can use that the mass flux is already known. To compute the advective energy flux it only has to be multiplied with the value of internal energy resulting after the Lagrangian step from Eq. (22),  $\tilde{\epsilon}_{i\pm 1/2}^m$  in the donor cell. For the radial direction, using Eq. (22), the following Eulerian update of the state variable  $(f^m \rho^m \epsilon^m)_{i+1/2}$  is found

$$(f^m \rho^m \epsilon^m)_{i+1/2}^{n+1} = (f^m \rho^m \epsilon^m)_{i+1/2}^n - \frac{\Delta t}{r_{i+1/2}(r_{i+1} - r_i)} \times [f_{i+1/2}^m p_{i+1/2}^{m,1/2} (r_{i+1} u_{i+1}^* - r_i u_i^*) + (\tilde{\epsilon}_{i+1}^m \Phi_{i+1}^m - \tilde{\epsilon}_i^m \Phi_i^m)]. \quad (34)$$

Again superscripts  $n$  and  $n+1$  denote subsequent time levels. It is emphasized, that this is the complete finite-volume update including the contribution of the Lagrangian step (i.e. the first term in the square brackets). Upwind values  $\tilde{\epsilon}_i^m$  appearing in the advective flux

$$\tilde{\epsilon}_i^m := \begin{cases} \tilde{\epsilon}_{i-1/2}^m, & u_i^* > 0 \\ \tilde{\epsilon}_{i+1/2}^m, & u_i^* \leq 0 \end{cases}, \quad (35)$$

are evaluated with the help of Eq. (22). We omit the modifications for the  $z$ -direction here because these are almost trivial.

#### 3.4.3. Radial momentum advection

The new momenta obtained during the Lagrangian step have to be redistributed onto the original Eulerian grid. Momentum advection on a staggered grid follows ideas outlined by Benson (1992) [1]. This demands to associate a mass (per unit radian and length in  $z$ -direction) with the  $i$ th node of the momentum grid, which we obtain by multiplying the definition of  $(\rho\Delta r)_i$  in Eq. (21) by  $r_i$ , rewritten in the form

$$M_i := r_i [\rho_{i+1/2}(r_{i+1/2} - r_i) + \rho_{i-1/2}(r_i - r_{i-1/2})] = \frac{1}{2} [M_{i+1/2}(1 - \zeta_{i+1/2}) + M_{i-1/2}(1 + \zeta_{i-1/2})], \quad (36)$$

where the auxiliary quantities  $\zeta_{i+1/2}$  and  $\Delta r_{i+1/2}$  are given by

$$\zeta_{i+1/2} := \frac{1}{2} \frac{\Delta r_{i+1/2}}{r_{i+1/2}}, \quad \Delta r_{i+1/2} := r_{i+1} - r_i, \quad (37)$$

and  $M_{i+1/2}$  is the cell mass per unit radian and length  $\Delta z$  in  $z$ -direction

$$M_{i+1/2} := \rho_{i+1/2} r_{i+1/2} \Delta r_{i+1/2}. \quad (38)$$

Note that  $M_i$  is a weighted average of adjacent cell masses  $M_{i\pm 1/2}$  such that redistribution of mass is conservative despite it is not based on a control volume. One can think of a number of different averages based on a control volume in between two radii that may be cell centres or centre-of-mass coordinates of the cells. In either case an average in the form of Eq. (36) results, the only change being a redefinition of  $\zeta_{i\pm 1/2}$ . For example, a  $M_i$  based on a control volume in between  $r_{i-1/2}$  and  $r_{i+1/2}$  will lead to  $\zeta_{i+1/2} := (1/4)\Delta r_{i+1/2}/r_{i+1/2}$ . The reasons to prefer our choice are that: (a) during the Lagrangian step in radial direction total energy associated with a node of the dual grid for momentum is conserved if the definition is as in

Eq. (36), see Appendix A for details, and (b) the behavior at the symmetry axis is correct. Now define the Eulerian mass flux across edge  $i$  by

$$\Phi_i := \sum_m \Phi_i^m. \quad (39)$$

With the help of (32), (33) follows that

$$M_{i+1/2}^+ = M_{i+1/2}^- + [\Phi_i - \Phi_{i+1}] \Delta t, \quad (40)$$

which is the Eulerian update of the cell mass where superscripts (+) and (−) distinguish values before and after the advection step. Carrying the definition of  $M_i$  in Eq. (36) over to the nodal mass  $M_i^+$  resulting after the remap step, leads to the following Eulerian update of nodal mass

$$M_i^+ = M_i^- + \frac{1}{2}[(1 + \zeta_{i-1/2})\Phi_{i-1} + (1 - \zeta_{i-1/2})\Phi_i] \Delta t - \frac{1}{2}[(1 + \zeta_{i+1/2})\Phi_i + (1 - \zeta_{i+1/2})\Phi_{i+1}] \Delta t. \quad (41)$$

This is in flux-difference form, i.e. conservative, when a mass flux on the momentum grid is identified with

$$\Phi_{i+1/2} := \frac{1}{2}[(1 + \zeta_{i+1/2})\Phi_i + (1 - \zeta_{i+1/2})\Phi_{i+1}]. \quad (42)$$

In the last formula, the weight factors contain the effect of curvilinear coordinates. Interestingly, specializing to  $i = 0$ , there is no contribution from  $\Phi_1$  due to the value of  $\zeta_{1/2} = 1$ . Moreover  $\Phi_0 = 0$  at the symmetry axis, so  $\Phi_{1/2} = 0$  is compatible with the requirement that the radial momentum at the symmetry axis remains zero. A different form of the weight factors would violate this condition. The momentum remap equation is then

$$M_i^+ u_i^+ = M_i^- \tilde{u}_i + [\Phi_{i-1/2} \hat{u}_{i-1/2} - \Phi_{i+1/2} \hat{u}_{i+1/2}] \Delta t, \quad (43)$$

where  $\hat{u}_{i+1/2}$  is a second-order interpolation of the velocity at the end of the Lagrangian step,  $\tilde{u}_i$ . The following value of the interpolated velocity  $\hat{u}_{i+1/2}$  is currently chosen

$$\hat{u}_{i+1/2} = \begin{cases} \tilde{u}_i + \Delta_{i+1/2} u \left( \frac{M_i - \Phi_{i+1/2} \Delta t}{2M_i} \right), & \Phi_{i+1/2} > 0 \\ \tilde{u}_{i+1} - \Delta_{i+1/2} u \left( \frac{M_{i+1} - \Phi_{i+1/2} \Delta t}{2M_{i+1}} \right), & \Phi_{i+1/2} \leq 0 \end{cases}. \quad (44)$$

The expression  $\Delta_{i+1/2} u$  is the monotonized difference

$$\Delta_{i+1/2} u := \begin{cases} [\tilde{u}_i - \tilde{u}_{i-1}] \Psi \left( \frac{\tilde{u}_{i-1} - \tilde{u}_{i-2}}{\tilde{u}_i - \tilde{u}_{i-1}} \right), & \Phi_{i+1/2} > 0 \\ [\tilde{u}_{i+1} - \tilde{u}_i] \Psi \left( \frac{\tilde{u}_i - \tilde{u}_{i-1}}{\tilde{u}_{i+1} - \tilde{u}_i} \right), & \Phi_{i+1/2} \leq 0 \end{cases}, \quad (45)$$

here  $\Psi$  is the flux limiter function. There are currently four possible choices for the flux limiter function: minmod, superbee, van Leer, monotonized centred. These choices are compared in the numerical examples section. To derive the particular form of interpolation for the velocity  $\hat{u}_{i+1/2}$ , we first define the following auxiliary velocity

$$u_{i+1/2} := \begin{cases} \frac{\Delta r}{M_i} \Phi_{i+1/2}, & (\Phi_{i+1/2} > 0) \\ \frac{\Delta r}{M_{i+1}} \Phi_{i+1/2}, & (\Phi_{i+1/2} \leq 0) \end{cases}. \quad (46)$$

The velocity  $u_{i+1/2}$  is interpreted as the value along the particular streamline that reaches the position  $r_{i+1/2}$  at the end of the Lagrangian step. For positive values of  $\Phi_{i+1/2}$  the domain of dependence is the interval  $\{r_{i+1/2} - u_{i+1/2} \Delta t; r_{i+1/2}\}$ , otherwise it is  $\{r_{i+1/2}; r_{i+1/2} - u_{i+1/2} \Delta t\}$ . The interpolation of the velocity  $\tilde{u}$  resulting after the Lagrangian step is linear

$$\tilde{u}(r) = \begin{cases} \tilde{u}_i + \frac{r-r_i}{\Delta r} \Delta_{i+1/2} u, & (\Phi_{i+1/2} > 0) \\ \tilde{u}_{i+1} + \frac{r-r_{i+1}}{\Delta r} \Delta_{i+1/2} u, & (\Phi_{i+1/2} \leq 0) \end{cases}, \quad (47)$$

where  $\Delta_{i+1/2} u$  is monotonized as explained above and  $r$  is a Lagrangian coordinate. Now we evaluate the average of  $\tilde{u}(r)$  over the domain of dependence

$$\hat{u}_{i+1/2} := \begin{cases} \int_{r_{i+1/2}-u_{i+1/2}\Delta t}^{r_{i+1/2}} \tilde{u}(r) dr / \left( \int_{r_{i+1/2}-u_{i+1/2}\Delta t}^{r_{i+1/2}} dr \right), & (\Phi_{i+1/2} > 0) \\ \int_{r_{i+1/2}}^{r_{i+1/2}-u_{i+1/2}\Delta t} \tilde{u}(r) dr / \left( \int_{r_{i+1/2}}^{r_{i+1/2}-u_{i+1/2}\Delta t} dr \right), & (\Phi_{i+1/2} \leq 0) \end{cases}. \quad (48)$$

The result of the integration in the case ( $u_{i+1/2} > 0$ ) is

$$\begin{aligned} \hat{u}_{i+1/2} &= \tilde{u} \left( r_i + \frac{1}{2} (\Delta r - u_{i+1/2} \Delta t) \right) \\ &= \tilde{u}_i + \frac{M_i - \Phi_{i+1/2} \Delta t}{2M_i} \Delta_{i+1/2} u, \end{aligned} \quad (49)$$

where (47) has been used. The other case ( $u_{i+1/2} \leq 0$ ) is analogous; one reproduces the formula for  $\hat{u}_{i+1/2}$ , Eq. (44). The above derivation is not fully satisfying for cylinder coordinates because one should have a volume average over the domain of dependence instead. But additional terms are of a higher order in  $\Delta t$ , so it can be justified omitting them.

#### 3.4.4. Transverse momentum advection

A difficult aspect of the spatially staggered discretization is that velocity components are attached to different edges of the cell. The transverse velocity component  $v_{i+1/2,j}$  is associated with the lower cell edge, see Fig. 1. There is no change in transverse velocity during the Lagrangian step; accelerations acting in  $z$ -direction are considered during the substep for the  $z$ -direction. Only advective effects have to be taken into account for the  $z$ -momentum during the substep in  $r$ -direction. For the Eulerian remap step, the control volume for  $v_{i+1/2,j}$  is defined as the region  $\{r_i; r_{i+1}\} \times \{z_{j-1/2}; z_{j+1/2}\}$  where  $z_{j\pm 1/2} := (z_j \pm z_{j\pm 1})/2$  are the  $z$ -coordinates of centres of two vertically adjacent cells. The corresponding mass in the control volume is obtained as

$$M_{i+1/2,j} := \frac{1}{2} (M_{i+1/2,j+1/2} + M_{i+1/2,j-1/2}), \quad (50)$$

in terms of the cell masses (these definitions assume an equidistant mesh in the  $z$ -direction). There is no  $r$ -dependent weight because both vertically adjacent cells used in the definition have the same radial coordinates. Accepting the same weighting formula for the mass following after advection the mass flux in radial direction through a face centred at  $(r_i, z_j)$  follows from

Eq. (40)

$$\Phi_{i,j} := \frac{1}{2}(\Phi_{i,j+1/2} + \Phi_{i,j-1/2}). \quad (51)$$

The update of mass and momentum are given by

$$M_{i+1/2,j}^+ = M_{i+1/2,j}^- + (\Phi_{i,j} - \Phi_{i+1,j})\Delta t, \quad (52)$$

$$M_{i+1/2,j}^+ v_{i+1/2,j}^+ = M_{i+1/2,j}^- v_{i+1/2,j}^- + (\Phi_{i,j} \hat{v}_{i,j} - \Phi_{i+1,j} \hat{v}_{i+1,j})\Delta t, \quad (53)$$

where  $\hat{v}_{i,j}$  is a monotonized linear interpolation, in analogy to that in Eq. (44). During the  $z$  substep of the dimensionally split algorithm the velocity components interchange their longitudinal and transversal character. There are a few more or less trivial modifications which we do not list here for brevity.

#### 4. Volume-of-fluid method

##### 4.1. Overview

The implementation of the piecewise linear volume-of-fluid method is independent of other parts of the algorithm. It only requires the knowledge of time-averaged velocities at the edges. For a detailed review of such methods see Rider and Kothe [2], Gueyffier et al. [3], Pilliod and Puckett [4], Benson [5], or Aulisa et al. [15]. The volume-of-fluid algorithm consists of three parts: interface reconstruction, Lagrangian translation and deformation of interfaces, and the Eulerian transport (or advection) calculation. The reconstruction here is carried out on the fixed Eulerian grid. In multi-material cells an interface normal direction between materials has to be found using volume fractions in a neighborhood. Following Gueyffier et al. [3], the normal direction is given as an approximation of the gradient of volume fraction using a 9-cell stencil, here. As soon as there are more than two materials in a cell, a material order has to be defined during advection, and the interfaces have to be mutually non-intersecting. How to achieve this, is described for the case of three materials only. During the Lagrangian step, a deformation of material interfaces takes place, which may be written as a transformation of the equation for the interface line [3]. The Eulerian advection or remap step subsequently has to redistribute the volume of each material in the overlap region between the Lagrangian and Eulerian grids onto the original Eulerian grid.

##### 4.2. Piecewise linear reconstruction in cylindrical coordinates

The equation of the material interface in a multi-material cell is

$$n_r(r - r_i) + n_z(z - z_i) = \alpha, \quad (54)$$

such that the fluid is occupying the crosshatched polygon under the line as indicated in Fig. 2. The choice of Gueyffier et al. [3] for the finite difference approximation of the gradient of volume fraction is equivalent to the procedure of, first, computing averages of four cells adjacent to a vertex and second, using these vertex averages  $f_{i,j}^m$  to obtain cell-centred estimates of

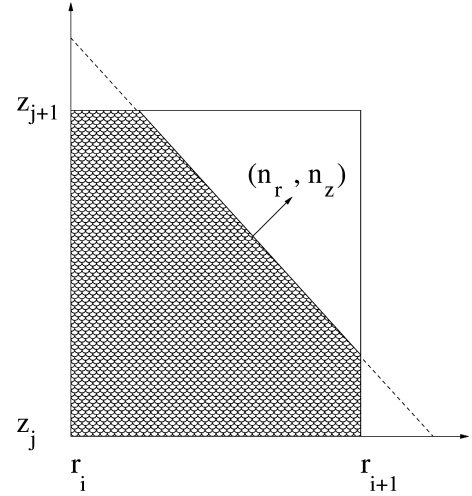


Fig. 2. Geometry of linear interface reconstruction in cell  $(i + 1/2, j + 1/2)$ .

the gradient with the sign corresponding to an outward-directed normal. There are improved methods for an estimate of the normal, see [4,5], but they are computationally more demanding and require to solve a least squares problem. Further, they need multiple inversions of Eq. (55) below to find the constant of the line,  $\alpha$ . These methods are second-order accurate in the sense that, if the actual material interface is a straight line, it is exactly reproduced.

The parameter  $\alpha$  has to be found from the condition that the volume of the crosshatched polygon in Fig. 2 is equal to the volume of material  $m$  as computed from  $f^m$  in the particular cell (if there are no more than two materials, otherwise there is a group of materials in the crosshatched polygon). In cylinder geometry, Eq. (11) of Gueyffier et al. [3] is generalized for the volume of fluid in a rectangular region with origin  $r_i$  in radial direction, length  $\Delta r$  and height  $\Delta z$

$$V(n_r, n_z, \alpha, \Delta r, \Delta z, r_i) := f_{i+1/2,j+1/2} r_{i+1/2} \Delta r \Delta z = \frac{1}{2n_r n_z} \left[ \alpha^2 \left( r_i + \frac{\alpha}{3n_r} \right) - \Theta(\alpha - n_r \Delta r) (\alpha - n_r \Delta r)^2 \left( r_{i+1} + \frac{(\alpha - n_r \Delta r)}{3n_r} \right) - \Theta(\alpha - n_z \Delta z) (\alpha - n_z \Delta z)^2 \left( r_i + \frac{(\alpha - n_z \Delta z)}{3n_r} \right) \right], \quad (55)$$

where  $\Theta$  denotes the Heaviside step function. Note that a factor of  $2\pi$  is always omitted. The derivation is analogous to [3] with the only difference that the volume of a ring with triangular cross section in cylinder coordinates is

$$V_{ABC} = \pi \frac{(r_A + r_B + r_C)}{3} \times (r_A(z_B - z_C) + r_B(z_C - z_A) + r_C(z_A - z_B)). \quad (56)$$

The formula (55) is valid for standard orientation, i.e. positive components of the normal, only. If  $n_r < 0$  one has to substitute  $n_r \rightarrow |n_r| \Delta r$ ,  $\alpha \rightarrow \alpha + |n_r|$  and interchange  $r_i$  and  $r_{i+1}$  in Eq. (55) and likewise if  $n_z < 0$  one substitutes  $n_z \rightarrow |n_z|$  and  $\alpha \rightarrow \alpha + |n_z| \Delta z$ . The problem of the determination of  $\alpha$  leads



to a linear, quadratic or cubic equation that is solved analytically. Special care is necessary in the case of a cubic equation if the solution in terms of trigonometric functions may degrade accuracy. In such a case a series expansion of the analytical formula for the cubic root in terms of the coefficients of the cubic equation is used; typically this occurs when volume fractions are close to zero or one. A relative error for the volume of no more than twenty times the machine accuracy (in double precision) can be achieved in this way. Because our algorithm is able to handle huge density ratios this detail has been found to be important.

The six-parametric function defined in Eq. (55) can be used to evaluate a material volume in any rectangular region not necessarily coinciding with a computational cell if the interface line parameters are given with respect to  $r_i$  as the origin. We did not actually implement Eq. (55) to evaluate the transport volumes in the domain of dependence of the advection equation. Instead, an algorithm due to Rider and Kothe [2] is used, which explicitly constructs the points of the polygon enclosing the fluid in a rectangular region given the interface line parameters. Testing each vertex of the bounding rectangle on which side of the interface line it is situated, is sufficient. If two subsequent vertices are on different sides an intersection point on the interface line is constructed. Note that this construction will never lead to a division by zero because the decision about the location of two subsequent vertices relative to the interface leads to a nonzero distance among subsequent polygon points. With the help of the polygon points one can compute the enclosed volume. This is numerically more robust than Eq. (55) and automatically covers all possible orientations and degenerate cases (where one component of the normal vanishes).

#### 4.3. Material advection I: Lagrangian step

Having reconstructed the material interface in each cell the next problem is to investigate the effect of the Lagrangian step on the material volume. It is emphasized that the final algorithm is purely Eulerian, so the considerations in this subsection are merely to derive the Eulerian finite volume scheme for the volume fraction, see Eq. (68) below. For Cartesian coordinates Gueyffier et al. [3] obtained the Lagrangian deformation of the material interface in terms of a transformation formula for the interface line parameters. Using the time-averaged velocities  $u_i^*$  during the Lagrangian step and interpolating linearly the effect on the material interface is given by

$$\begin{aligned}\tilde{n}_r &= n_r \left( 1 + \frac{u_{i+1}^* - u_i^*}{\Delta r} \Delta t \right)^{-1}, \\ \tilde{m}_z &= m_z, \quad \tilde{\alpha} = \alpha + \tilde{n}_r u_i^* \Delta t,\end{aligned}\quad (57)$$

see [3]. These new line parameters are valid with respect to the old origin  $r_i$ . To investigate the effect of cylinder coordinates we introduce the concept of the radial centroid  $\hat{r}_m$  of material  $m$  defined by

$$\hat{r}_m A^m(n_r, n_z, \alpha, \Delta r, \Delta z) := V^m(n_r, n_z, \alpha, \Delta r, \Delta z, r_i), \quad (58)$$

such that  $\hat{r}_m$  is given in terms of the area filled by material  $m$  in the  $r$ - $z$  plane evaluated as the Cartesian equivalent of Eq. (55)

(see Eq. (11) of Gueyffier et al. [3]):

$$\begin{aligned}A(n_r, n_z, \alpha, \Delta r, \Delta z) \\ := \frac{1}{2n_r n_z} (\alpha^2 - \Theta(\alpha - n_r \Delta r)(\alpha - n_r \Delta r)^2 \\ - \Theta(\alpha - n_z \Delta z)(\alpha - n_z \Delta z)^2).\end{aligned}\quad (59)$$

Transformation to the new origin  $\tilde{r}_i = r_i + u_i^* \Delta t$  in the line equation leads to a further change  $\tilde{\alpha} \rightarrow \tilde{\alpha} - \tilde{n}_r u_i^* \Delta t = \alpha$ . This may be interpreted as: moving the mesh during the Lagrangian step in  $r$ -direction, the interface line transforms such that the so-called wetted area is invariant. The length in  $r$ -direction changes but it leaves the product  $\tilde{n}_r \Delta \tilde{r} = n_r \Delta r$  invariant. After these considerations the effect of the Lagrangian step on the “area of fluid” can be evaluated with the help of the explicit form of Eq. (59)

$$\begin{aligned}A(\tilde{n}_r, \tilde{n}_z, \tilde{\alpha} - \tilde{n}_r u_i^* \Delta t, \Delta \tilde{r}, \Delta z) \\ = \left( 1 + \frac{(u_{i+1}^* - u_i^*)}{\Delta r} \Delta t \right) A(n_r, n_z, \alpha, \Delta r, \Delta z).\end{aligned}\quad (60)$$

Unfortunately, the *volume* of fluid does not merely change by a simple factor. During the Lagrangian step the velocity field is approximated by a linear interpolation, so any material point  $r \in \{r_i; r_{i+1}\}$  moves according to

$$\tilde{r} = r + u_i^* \Delta t + \frac{r - r_i}{\Delta r} (u_{i+1}^* - u_i^*) \Delta t. \quad (61)$$

Applying this for the centroid of material  $m$  one has

$$\hat{\tilde{r}}_m = \hat{r}_m \left( 1 + \frac{(u_{i+1}^* - u_i^*) \Delta t}{\Delta r} \right) - \frac{(r_i u_{i+1}^* - r_{i+1} u_i^*) \Delta t}{\Delta r}. \quad (62)$$

Multiplying the last equation by (60), the new volume of material  $m$  is found. After lengthy but trivial algebraic manipulations this yields the Lagrangian change of material volume

$$\begin{aligned}\tilde{V}_{i+1/2}^m &= \left( 1 + \frac{(u_{i+1}^* - u_i^*) \Delta t}{\Delta r} \right) \left( 1 + \frac{(u_{i+1}^* + u_i^*) \Delta t}{2r_{i+1/2}} \right) V_{i+1/2}^m \\ &\quad - \left( 1 + \frac{(u_{i+1}^* - u_i^*) \Delta t}{\Delta r} \right) \frac{(r_i u_{i+1}^* - r_{i+1} u_i^*) \Delta t}{\Delta r} \\ &\quad \times \left[ A_{i+1/2}^m - \frac{V_{i+1/2}^m}{r_{i+1/2}} \right],\end{aligned}\quad (63)$$

where the arguments of the volume and area functions have been omitted, but a cell index is retained, for clarity. We also attached a material superscript  $m$  to the above expressions to indicate that the line parameters for the particular material in question have to be used. Note that the first term on the right-hand side of Eq. (63) describes a homogeneous deformation by the factor

$$\begin{aligned}\left( 1 + \frac{(u_{i+1}^* - u_i^*) \Delta t}{\Delta r} \right) \left( 1 + \frac{(u_{i+1}^* + u_i^*) \Delta t}{2r_{i+1/2}} \right) \\ = \left( \frac{\tilde{r}_{i+1}^2 - \tilde{r}_i^2}{r_{i+1}^2 - r_i^2} \right).\end{aligned}\quad (64)$$

The second term in Eq. (63) arises due to both inhomogeneous distribution of material  $m$  and an  $r$ -dependent deformation. It

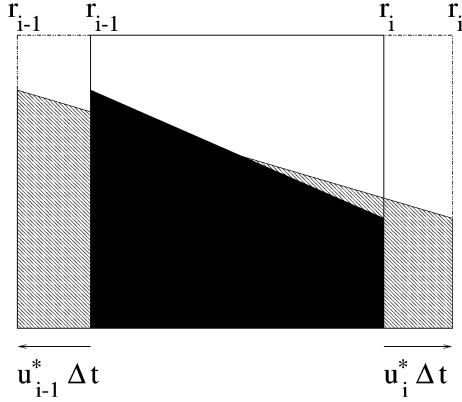


Fig. 3. Filled polygon: material 1 before Lagrangian step, hatched (partially obscured) polygon: after Lagrangian step.

is zero for fully present ( $f_{i+1/2}^m = 1$ ) or absent ( $f_{i+1/2}^m = 0$ ) materials and vanishes when summed over species. This particular term also vanishes if material interfaces are parallel to the  $r$ -axis.

#### 4.4. Material advection 2: Eulerian remap step

The Eulerian remap step requires the evaluation of a so-called transport or advected volume. This is the volume of material  $m$  in the overlap region between the old (Eulerian) and the new (Lagrangian) positions of the edges  $r_i$ , see Fig. 3. Let  $u_i^* > 0$ , then the donor cell is to the left of  $r_i$  (cell  $i - 1/2$ ). We compute the material interface after the Lagrangian step, using Eq. (57) with  $i \rightarrow i - 1$ . The formula for the line equation assumes that the origin is at  $r_{i-1}$ , the left boundary of the donor cell, but for the evaluation of the advected volume, the origin is at  $r_i$ . Thus the  $\alpha$  parameter is transformed by  $\tilde{\alpha} - \tilde{n}_r \Delta r = \alpha - n_r \Delta r + \tilde{n}_r u_i^* \Delta t$ . The length of the overlap region of the grid in radial direction is  $\tilde{r}_i - r_i = u_i^* \Delta t$ , which has to be substituted for the argument  $\Delta r$  in the 6-parametric function evaluating the volume of fluid, Eq. (55). So the complete expression for the volume of material  $m$  transported through edge  $i$  is

$$V_i^{m,(\text{adv})} = V_{i-1/2}^m(\tilde{n}_r, n_z, \alpha - n_r \Delta r + \tilde{n}_r u_i^* \Delta t, u_i^* \Delta t, \Delta z, r_i), \quad (65)$$

where the function on the right-hand side is given in Eq. (55). Additionally superscripts  $m$  and half-integer cell indices are attached to indicate that the interface parameters belong to material  $m$  and the left cell. The case  $u_i^* \leq 0$  with the right cell  $i + 1/2$  as the donor remains. Here, the origin of the rectangular overlap region is at  $r_i + u_i^* \Delta t < r_i$  so a shift is necessary:  $\tilde{\alpha} \rightarrow \tilde{\alpha} - \tilde{n}_1 u_i^* \Delta t = \alpha$ . With the convention, that advected volume has the sign of the velocity, the advected volume of material  $m$  for  $u_i^* \leq 0$  is

$$V_i^{m,(\text{adv})} = -V_{i+1/2}^m(\tilde{n}_r, n_z, \alpha, |u_i^*| \Delta t, \Delta z, r_i + u_i^* \Delta t). \quad (66)$$

Summing over species leads to the total volume of the overlap region

$$\sum_m V_i^{m,(\text{adv})} = \left( r_i + \frac{1}{2} u_i^* \Delta t \right) u_i^* \Delta t \Delta z, \quad (67)$$

irrespective of the sign of  $u_i^*$ . If  $k$  materials are present as donor only the first  $k - 1$  advected volumes are calculated. For the last transported material the advected volume is the complement of the others with respect to the total volume of the overlap region, (67). If there are more than two materials, all transport volume calculations are stacked in a certain order. This requires that interfaces form a non-intersecting onion skin model, see Benson [5]. A material order has to be found which is *unique for each cell*. This point is emphasized here because there are approaches where the material order may be different for each edge. In other words,  $V_i^{m,(\text{adv})}$  as given above is the sum of transport volumes of the group of materials “behind the  $m$ th interface”. The actual transport volume for the  $k$ th material,  $m_k$ , is then obtained by applying the above formulas for  $V_i^{m,(\text{adv})}$  for materials  $m_k$  and  $m_{k-1}$  and calculating differences. Likewise, the “area of fluid” is evaluated incrementally. It is now possible to collect the effect of the Lagrangian and Eulerian substeps in a single expression

$$\begin{aligned} (V_{i+1/2}^m)^{n+1} &= (V_{i+1/2}^m)^n + V_i^{m,(\text{adv})} - V_{i+1}^{m,(\text{adv})} \\ &\quad + \frac{(r_{i+1/2}^{1/2} u_{i+1}^* - r_i^{1/2} u_i^*) \Delta t}{r_{i+1/2} \Delta r} (V_{i+1/2}^m)^n \\ &\quad - \left( 1 + \frac{(u_{i+1}^* - u_i^*) \Delta t}{\Delta r} \right) \frac{(r_i u_{i+1}^* - r_{i+1} u_i^*) \Delta t}{\Delta r} \\ &\quad \times \left[ (A_{i+1/2}^m)^n - \frac{(V_{i+1/2}^m)^n}{r_{i+1/2}} \right], \end{aligned} \quad (68)$$

with  $r_i^{1/2} := r_i + u_i^* \Delta t / 2$  and superscripts  $n + 1$  and  $n$  denote subsequent time levels. The volume  $V_{i+1/2}^m$  can be eliminated in terms of volume fraction, but  $A_{i+1/2}^m$  is nontrivial and has to be evaluated from Eq. (59) using the geometric parameters obtained during interface reconstruction. Re-introducing volume fractions the above equation assumes a compact form when the following pseudo-fluxes (or fluctuations) are defined

$$\begin{aligned} F_i^{(\pm),m} &:= \frac{V_i^{m,(\text{adv})}}{r_{i\pm 1/2} \Delta z \Delta t} - \frac{r_i^{1/2} u_i^*}{r_{i\pm 1/2}} f_{i\pm 1/2}^m \\ &\quad + \frac{r_{i\pm 1/2} u_i^*}{r_{i\pm 1/2}} \left[ \frac{A_{i\pm 1/2}^m}{\Delta r \Delta z} - f_{i\pm 1/2}^m \right] \left( 1 + \frac{\Delta u_{i\pm 1/2}^* \Delta t}{\Delta r} \right), \end{aligned} \quad (69)$$

with the abbreviation  $\Delta u_{i\pm 1/2}^* := u_{i+1}^* - u_i^*$ . The complete Eulerian form of the discrete volume fraction advection equation in the radial substep of the dimensionally split algorithm is then simply given by

$$f_{i+1/2}^{m,n+1} = f_{i+1/2}^{m,n} + \frac{\Delta t}{\Delta r} [F_i^{(+),m} - F_{i+1}^{(-),m}]. \quad (70)$$

The advantage of the formulation is that the quantities  $F_i^{(\pm),m}$  only have to be evaluated one times at multi-material edges  $i$ . This avoids unnecessary calculations for trivial edges and produces an economic algorithm. Certain cases can be identified where trivial expressions for the advected volume arise, e.g., when a material is absent or fully present in the donor cell (but not necessarily on the other side). We take advantage of such a situation and avoid accuracy losses thereby. An edge  $i$  is said to

be trivial with respect to material  $m$  when at both sides either  $f_{i\pm 1/2}^m = 0$  or  $f_{i\pm 1/2}^m = 1$ . At trivial edges both  $F_i^{(\pm),m}$  vanish, as is easily shown, giving a rule to skip the calculation for absent materials and in a purely one-material situation.

For the  $z$ -direction of the dimensionally split algorithm we only list the expressions for the pseudo-fluxes  $F_j^{(\pm),m}$  here

$$F_j^{(\pm),m} := \frac{V_j^{m,(\text{adv})}}{r_{i+1/2}\Delta r\Delta t} - v_j^* f_{j\pm 1/2}^m, \quad (71)$$

where  $r_{i+1/2}$  is the radial cell centre common to the entire layer (we suppress an index  $i + 1/2$  common to the layer otherwise). These are used in the finite volume update of volume fraction in the form

$$f_{j+1/2}^{m,n+1} = f_{j+1/2}^{m,n} + \frac{\Delta t}{\Delta z} [F_j^{(+),m} - F_{j+1}^{(-),m}]. \quad (72)$$

The advected volume again depends on the sign of the velocity. If  $v_j^* > 0$ , it is evaluated as

$$V_j^{m,(\text{adv})} = V_{j-1/2}^m(n_r, \tilde{n}_z, \alpha - n_z\Delta r + \tilde{n}_z v_j^* \Delta t, \Delta r, v_j^* \Delta t, r_i), \quad (73)$$

whereas for  $v_j^* \leq 0$  it is given by

$$V_j^{m,(\text{adv})} = -V_{j+1/2}^m(n_r, \tilde{n}_z, \alpha, \Delta r, |v_j^*| \Delta t, r_i), \quad (74)$$

here  $r_i$  is the minimum radial coordinate common to all cells in the current row. Note that now the Lagrangian deformation in  $z$ -direction acts nontrivially on the  $z$ -component of the interface normal, e.g., in the case  $v_j^* > 0$  one has

$$\tilde{n}_z = n_z \left( 1 + \frac{v_j^* - v_{j-1}^*}{\Delta z} \Delta t \right)^{-1}. \quad (75)$$

In summary, a perfectly overshoot-free algorithm for material volume advection has been found, which is very economic and given in a closed algebraic form. In the case of solids, where a 0.1% deformation may already result in tensile failure, an overshoot-free treatment of such a material's volume is mandatory. The effect of cylinder coordinates has been worked out. The main additional cost as compared to Cartesian coordinates is the evaluation of terms containing the “area of fluid”  $A_{i+1/2}^m$  in the pseudo-fluxes.

#### 4.5. Advected mass

The definition of the mass flux, Eq. (32), appearing in the Eulerian step for cell-centred quantities contains the advected mass. In the  $r$ -direction deformation of material volume is inhomogeneous, so it is inconsistent to determine a spatially averaged density of material  $m$  after the Lagrangian step and to multiply it with the advected volume. Instead, we trace back the streamline reaching  $r_i$  at the end of the Lagrangian step to find the domain of dependence in radial direction. If velocity is interpolated linearly the velocity along this particular streamline is given by

$$\hat{u}_i := \begin{cases} u_i^* [1 + (u_i^* - u_{i-1}^*) \frac{\Delta t}{\Delta r}]^{-1}, & u_i^* > 0 \\ u_i^* [1 + (u_{i+1}^* - u_i^*) \frac{\Delta t}{\Delta r}]^{-1}, & u_i^* \leq 0 \end{cases}. \quad (76)$$

To derive this expression set  $\tilde{r} = r_i$  in Eq. (61), in the case  $u_i^* \leq 0$ , otherwise set  $\tilde{r} = r_{i+1}$  in Eq. (61) and shift indices  $i \rightarrow i - 1$ . Now the mass of material  $m$  flowing through edge  $r_i$  may be found by calculating the volume of the traceback region with the help of the interface parameters *before* the Lagrangian step and the initial mass density in the donor cell. For  $u_i^* > 0$ , the donor cell is at left, and the advected mass (per unit radian) found in this way is

$$M_i^{m,(\text{adv})} = \rho_{i-1/2}^m V_{i-1/2}^m(n_r, n_z, \alpha + n_r(\hat{u}_i \Delta t - \Delta r), \hat{u}_i \Delta t, \Delta z, r_i - \hat{u}_i \Delta t), \quad (77)$$

whereas for  $u_i^* \leq 0$  the donor cell is at the right and

$$M_i^{m,(\text{adv})} = -\rho_{i+1/2}^m V_{i+1/2}^m(n_r, n_z, \alpha, |\hat{u}_i| \Delta t, \Delta z, r_i). \quad (78)$$

Half-integer subscripts in the functions evaluating the material volume on the right-hand side indicate the donor cell to which the line parameters  $(n_r, n_z, \alpha)$ , appearing as arguments, belong. If there are more than two materials one has to compute the volumes multiplying  $\rho_{i\pm 1/2}^m$  incrementally, using material interfaces with the provision that the volume “behind the line” belongs to a sum of materials in transport order. The sum of all these volumes is equal to the total volume of the domain of dependence

$$\hat{V}_i = \hat{u}_i \Delta t \left( r_i - \frac{1}{2} \hat{u}_i \Delta t \right) \Delta z, \quad (79)$$

irrespective of the sign of  $u_i^*$ . The situation is analogous to the material order problem encountered for advected volume.

The way we compute advected masses, i.e. by characteristic traceback, ensures that never more mass of a material  $m$  than originally contained in the donor cell can be transported out. Because the advective flux of internal energy is constructed with the help of the mass flux it limits the advection of internal energy in the same way. This is a desired property in multi-material algorithms, where the situation may occur that all material of a species  $m$  is completely contained in the domain of dependence of advection. There is no way to improve the estimate for density in the donor cell beyond first order because this would lead to negative mass, possibly. In ordinary one-material numerical hydrodynamics, the CFL criterion for the time step suppresses the occurrence of a mass less than zero after advection.

#### 4.6. Onion skin order: Non-intersecting interface reconstruction

Presentations of VOF methods in the literature only treat the case of two materials where a unique solution exists and it does not matter which of the two materials in a cell is used to reconstruct their mutual interface [2,3]. In the general case, Benson [5,17] suggests to determine a “material order” and then to perform the reconstruction of the interface recursively, he calls this the “onion skin model”, see Fig. 4. Any intersection of material interfaces within the cell would induce overshoots into the geometry-based advection scheme for material volume. To the best of our knowledge, none of the treatments of VOF

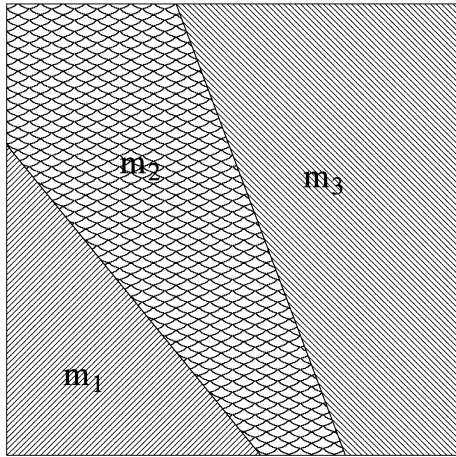


Fig. 4. Onion skin order of material interfaces in a computational cell.

methods in the literature offers a solution to this problem of a non-intersecting partition of the cell. It is clear that the complexity of intersections grows with the number of materials. In the absence of a general solution, here we describe our method that works in the case of three materials.

The first step in our algorithm is to carry out an independent interface reconstruction for each material individually. We proceed from the volume fraction in a nine-cell stencil. With each vertex of the central cell we associate a volume fraction computed as average of four cells adjacent to the vertex. These averages are differenced to determine the normal of the interface line as estimate of the gradient of volume fraction, for each of the materials. Thereafter the line constant  $\alpha$  is determined such that the volume “behind the line” for each material is matched individually. This only relies on two-material logics of estimating a normal to the interface and solving the equation for the line constant  $\alpha$ . For three materials, only two interface lines are required to partition the computational cell uniquely.

Table 1

Cases of intersection among pairs of interface lines

Case	Lines of 3 and 1	Lines of 2 and 3	Lines of 1 and 2	Reaction
0	0	0	0	reject 1, 2 or 3
1	0	0	1	reject 1 or 2
2	0	1	0	reject 2 or 3
3	0	1	1	reject 2
4	1	0	0	reject 1 or 3
5	1	0	1	reject 1
6	1	1	0	reject 3
7	1	1	1	adjust normal

So the interface construction for one material may be forgotten, this material is “sandwiched” in between the two others. The decision is simple when no intersection point between individual lines found above occurs in the given cell, otherwise it is more complicated.

Therefore, the second step is to test for an intersection point of each pair of interface lines in a cell. The aim is to retain two out of three interface lines to partition the cell into an “onion skin”. Counting each intersection among a particular pair of interface lines independently, there are  $2^3 = 8$  different cases that are conveniently numbered by an integer from 0 to 7, see Table 1. In the columns of Table 1 values of one and zero indicate intersection or no intersection, respectively.

The third step is to reject the interface construction of one of the materials, as indicated in the last column of Table 1. In the case of multiple choices for discarding an interface, the method for the selection is explained below. Only in case 7 all single-material interface reconstructions are incompatible, and there is the need to adjust the direction of at least one interface normal.

In the three cases where two intersections occur, i.e. 3, 5, and 6, it is sufficient to reject just the particular interface line intersecting the two others. Fig. 5 displays two examples of

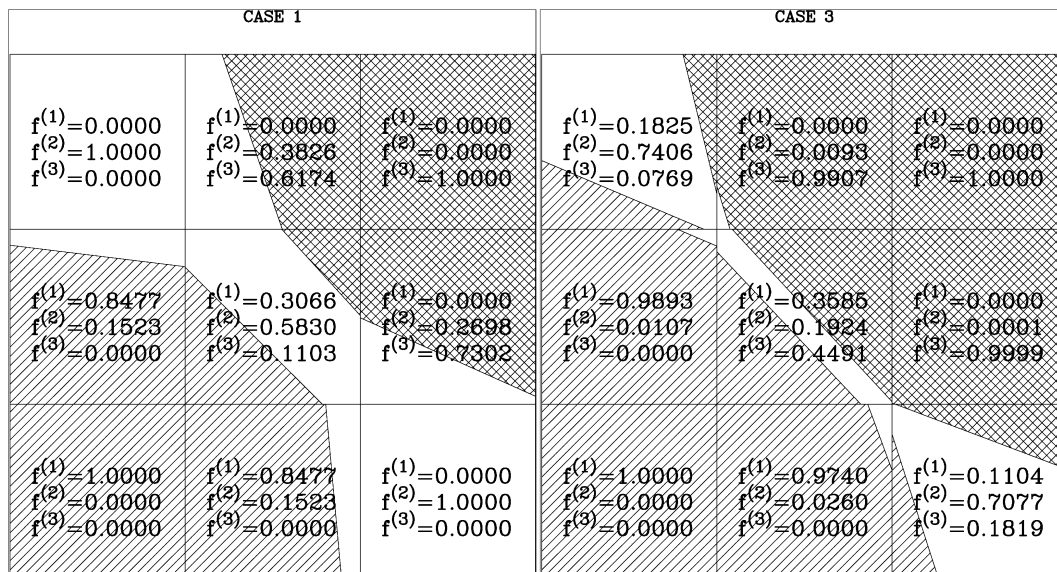


Fig. 5. Example 3-material interface reconstruction. Left: case 1. Right: case 3. In central cell, material 3 occupies crosshatched triangle at upper right vertex, material 1 occupies hatched triangle at lower left vertex; material 2 (white) lies in between.



three-material interface reconstruction. In the left part, Fig. 5 shows an example of case 1 occurring in the central cell. The interface lines of materials 1 and 2 would intersect. The overlap test, see below for details, reveals that the polygonal regions occupied by materials 1 and 3 are non-overlapping, whereas the regions of material 2 and 3 would overlap. Therefore, the interface line of material 2 is rejected and this material appears in the six-vertex polygonal region in between the two others in the central cell in the left part of Fig. 5. In the three cases with only one intersection, 1, 2, and 4, a choice has to be made which one from a pair of intersecting interface lines to reject. The appropriate condition is that the remaining two materials occupy disjoint polygonal regions. The test is simple, noting that each polygon associated with a material has to contain at least one vertex of the computational cell, because an interface line cuts out at least a triangle from a rectangular cell. By definition, all points of the polygonal region associated with material  $k$  share the property to be located on the same side of the interface line  $k$ , expressed as

$$n_r^{(k)}(r - r_i) + n_z^{(k)}(z - z_j) \leq \alpha^{(k)}, \quad (80)$$

remember that the normal points outward. If there is a cell vertex belonging to two different polygonal regions at the same time, it is located at the same side of each of the interface lines. So it is necessary to test the above inequality for all vertices of the cell, using the line parameters of the two interfaces in question. Two polygonal regions could have an overlap not containing a cell vertex at all, but then there has to be an intersection of interface lines within the cell, which was excluded. Sometimes the disjointness test is non-decisive, i.e. it does not eliminate any of the interfaces of the intersecting pair. In such a non-decisive outcome, a priority rule is applied. For instance, if one material is a gas, and the other is a solid, the interface of the gas is to be omitted; this could alternatively be decided dynamically, by comparing the bulk modulus of the materials and selecting the least “stiff” material. The material belonging to the rejected interface is again “sandwiched” in between the two others. In the second example depicted in Fig. 5, which illustrates case 3, the interface line of material 2 in the central cell would intersect those of materials 1 and 3 and is rejected. As the result, the crosshatched triangle at the upper right corner of the central cell belongs to material 3, and material 1 occupies the hatched triangle at the lower left corner of the same cell; material 2 fills the empty region in between materials 1 and 3.

In case 0 there are three candidate interface lines to discard. We select the pair (1, 2) and test if the respective fluids occupy disjoint regions, as described above. If disjoint, the interface construction of material 3 is rejected. Otherwise, the pair (2, 3) is tested, and if disjoint, the interface line of material 1 is omitted. The remaining possibility is to discard the interface line of material 2. Note that the order of these tests can be arranged such that omission of the interface line of the least “stiff” material is preferred. In this way, a priority rule is included into case 0.

In case 7, where all three interfaces intersect, we use a heuristic procedure to decrease the misalignment. First we or-

der the materials in decreasing volume fraction, such that material  $k1$  has the largest volume fraction. Denote the interface normals by  $\mathbf{n}_{k1} \dots \mathbf{n}_{k3}$ . Then we calculate the scalar product  $\mathbf{n}_{k1} \cdot \mathbf{n}_{k3}$ . If the scalar product is negative, we determine a new interface normal for material  $k3$  by

$$\mathbf{n}'_{k3} = \frac{1}{|\mathbf{n}_{k1}|} \mathbf{n}_{k3} - \frac{1}{|\mathbf{n}_{k3}|} \mathbf{n}_{k1}. \quad (81)$$

The construction ensures that for a material  $k3$  with low volume fraction in the cells contributing to the gradient approximation the new normal does not deviate too much from the anti-normal direction of the most abundant material. Recall that the normal vectors are approximations to the gradients of volume fractions, not unit vectors. The modulus of a normal vector becomes small when the volume fraction of this material in the cells contributing to the gradient approximation is low. If the scalar product  $\mathbf{n}_{k1} \cdot \mathbf{n}_{k3}$  is positive, we determine  $\mathbf{n}_{k1} \cdot \mathbf{n}_{k2}$ . If the latter is negative, we modify the normal  $\mathbf{n}_{k2}$  analogously, using (81) with the substitution  $k3 \rightarrow k2$ . If both previous scalar products are positive, the normal of material  $k3$  is modified making the substitution  $k1 \rightarrow k2$  in (81). Thereafter, we reconstruct the interface for the material whose normal has been changed, and evaluate intersections among pairs of material interface lines another time. Eventually, this time there are fewer than three intersections, so the case 7 disappears, otherwise re-alignment of interfaces has to go on as described. This needs no more than 1–2 iterations typically. If each of the eight different cases listed in Table 1 were equally probable, in the 87.5% of the other cases we avoid to run through the interface reconstruction process for one material twice.

So far we have only described the non-degenerate case of three materials in the cell under consideration. If the cell contains only two materials, their interface normals arising as gradient approximations are not necessarily collinear, if at least one of the cells in the stencil used for the gradient approximation contains a third material. There are various possibilities to deal with such a situation, e.g., based on a priority list, such that one of the two materials is more important, so the interface construction for this material is always accepted. Another workaround, which we prefer, is to omit the third material that is absent in the given cell in the vertex-averages leading to the gradient approximation. In other words, these vertex averages are re-normalized such that the sum over species is one, omitting the third material, leading to uniqueness of the interface normal. We are aware of different approaches to material ordering [5,17], but the important technical detail how to avoid intersections is missing in the literature. Our solution to the “onion skin” order problem does not depend on the details how interface normals are estimated during the reconstruction step. It also embeds a priority rule in the sense that the interface construction of certain materials is rejected more likely. Unfortunately, our scheme has no obvious extension to more than three materials. The complexity grows exponentially, so there are  $2^{N(N-1)/2}$  different cases of intersection for  $N$  materials, and a treatment on a case-by-case basis seems to be impossible for large  $N$ . More effort is necessary to find acceptable solutions in the case of more materials.



VOF INTERFACE RECONSTRUCTION T= 0.00000E+00 CYCLE 0

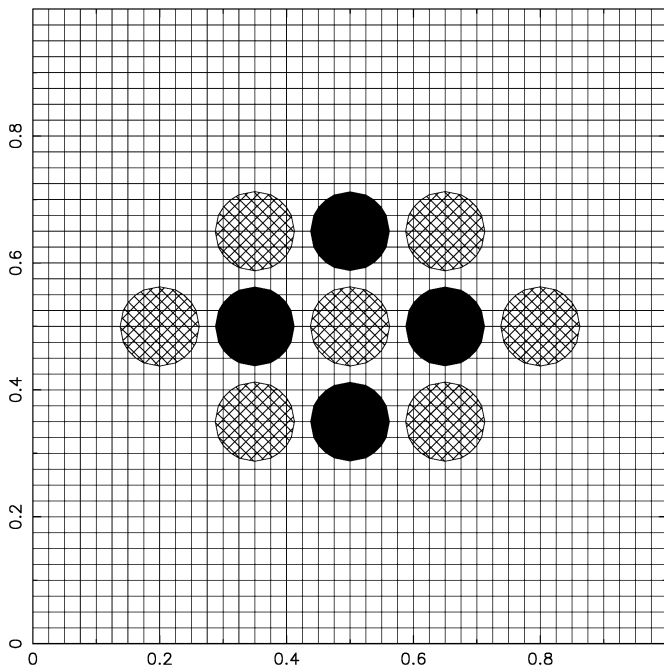


Fig. 6. Pure advection test, initial configuration with three materials.

## 5. Numerical examples

### 5.1. Pure advection of a three-material configuration

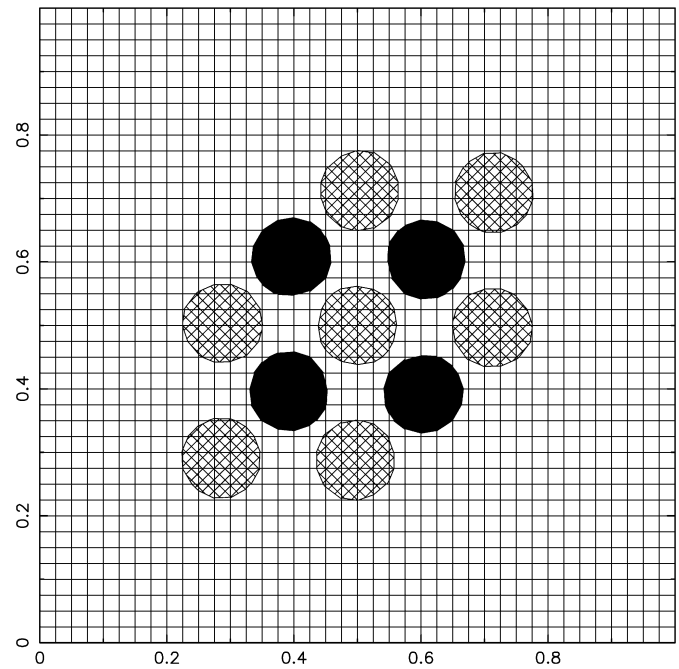
To test the VOF advection scheme for three materials we investigated two problems in Cartesian coordinates on a unit square domain. The first example is set up on a grid of  $40^2$  cells. The initial configuration shown in Fig. 6 represents an arrangement of spheres consisting of two different materials, embedded in a third material. The example is a test of pure advection in a given velocity field corresponding to uniform rotation  $v_x = \Omega(y - y_0)$ ,  $v_y = -\Omega(x - x_0)$  with angular frequency  $\Omega = 1$  around a centre located at  $x_0 = y_0 = 0.5$ . We used a variant of our advection algorithm valid for Cartesian coordinates in the test. After approximately 135 degrees of rotation, corresponding to 117 cycles of the algorithm at a CFL number of  $\sim 0.5$ , the situation in Fig. 7 is reached. The material boundaries of the individual spheres still are continuous and the shapes are preserved, to a good degree of approximation. Also, the sphere in the centre is nearly invariant.

The second example involves shear and distortion acting on the same initial configuration as in Fig. 6. We selected the so-called deformation field with the stream function given by

$$\Psi = \frac{1}{4\pi} \cos\left(2\pi \frac{t}{T}\right) \sin\left(4\pi \left(x + \frac{1}{2}\right)\right) \cos\left(4\pi \left(y + \frac{1}{2}\right)\right), \quad (82)$$

corresponding to Eq. (14) of [2] multiplied by a time-dependent periodic factor with period  $T$  (velocities follow as  $v_x = -\partial\Psi/\partial y$  and  $v_y = \partial\Psi/\partial x$ ). Ideally, the numerical solution should return to the initial configuration at multiples of a half period [2]. The larger the period  $T$ , the more severe is the deformation at intermediate times. We simulated examples with

VOF INTERFACE RECONSTRUCTION T= 2.35619E+00 CYCLE 117

Fig. 7. Pure advection test with three materials, velocity corresponds to uniform rotation with angular velocity  $\Omega = 1$ , situation after rotation by approximately 135 degrees.

$T = 1.0, 1.5, 2.0$  and compared the solution at multiples of an half-period ( $t/T = 0.5, 1.0, 1.5, 2.0$ ) to the initial state. The grid resolution varied from  $40^2$  to  $160^2$ . As measure of the error we took the  $L_1$  norm, see Eq. (17) of [2] and, because there are more than two materials, evaluated the error for the volume fractions  $f^{(1,2)}$  of the two “foreground” materials contained in the spheres, see Fig. 6, separately. Tables 2–4 show the results. Our initial configuration is much more complicated than the rotationally invariant one of [2], so absolute values of the error should not be compared. In Fig. 8 we display the solution with a period of  $T = 1.5$  in the moment of largest distortion at  $t/T = 0.25$  in  $160^2$  resolution. The cross-hatched spheres initially at left and right in the central row experience tearing and splitting and so does the black sphere initially at the centre in the lower row in Fig. 6. The solution resulting after two periods is shown in Fig. 9. No intrusion of the two foreground materials into each other occurred although there is some background material inside the upper and lower black spheres in the central part.

### 5.2. 1D stiffened gas shock tube

The following shock tube problem due to [26] has been selected by a number of authors to validate their method in the one-dimensional case, see [28–30]. The left state in the shock tube is water with density  $\rho = 1000 \text{ kg m}^{-3}$  at  $P = 10^9 \text{ Pa}$  modeled as a stiffened gas

$$P = (\gamma - 1)\rho\epsilon - \gamma K, \quad (83)$$

where  $\gamma = 4.4$  and  $K = 0.6 \times 10^9 \text{ Pa}$ . The right state is dense air with  $\rho = 50 \text{ kg m}^{-3}$  at a pressure of  $10^5 \text{ Pa}$  described as

Table 2

$L_1$ -norm error of volume fractions  $f^{(1,2)}$  for advection in deformation velocity field as function of grid resolution and time. Period:  $T = 1.0$

Variable	$f^{(1)}$	$f^{(1)}$	$f^{(1)}$	$f^{(1)}$
Grid	$t/T = 0.5$	$t/T = 1.0$	$t/T = 1.5$	$t/T = 2.0$
$40^2$	0.00735177	0.00991429	0.0134862	0.0178515
$80^2$	0.00399739	0.00476526	0.0072676	0.0094218
$160^2$	0.00214842	0.00240961	0.0037335	0.0047976

Variable	$f^{(2)}$	$f^{(2)}$	$f^{(2)}$	$f^{(2)}$
Grid	$t/T = 0.5$	$t/T = 1.0$	$t/T = 1.5$	$t/T = 2.0$
$40^2$	0.0194554	0.0147611	0.0240999	0.0250373
$80^2$	0.0106186	0.0064253	0.0128978	0.0121902
$160^2$	0.0055353	0.0028049	0.0065629	0.0055540

Table 3

$L_1$ -norm error of volume fractions  $f^{(1,2)}$  for advection in deformation velocity field as function of grid resolution and time. Period:  $T = 1.5$

Variable	$f^{(1)}$	$f^{(1)}$	$f^{(1)}$	$f^{(1)}$
Grid	$t/T = 0.5$	$t/T = 1.0$	$t/T = 1.5$	$t/T = 2.0$
$40^2$	0.00941987	0.0132004	0.0188588	0.0256867
$80^2$	0.00522345	0.0065336	0.0106140	0.0123715
$160^2$	0.00274688	0.0031988	0.0053033	0.0061758

Variable	$f^{(2)}$	$f^{(2)}$	$f^{(2)}$	$f^{(2)}$
Grid	$t/T = 0.5$	$t/T = 1.0$	$t/T = 1.5$	$t/T = 2.0$
$40^2$	0.0233749	0.0245906	0.0352202	0.0353180
$80^2$	0.0120263	0.0075784	0.0149540	0.0148963
$160^2$	0.0066079	0.0033708	0.0079029	0.0066659

Table 4

$L_1$ -norm error of volume fractions  $f^{(1,2)}$  for advection in deformation velocity field as function of grid resolution and time. Period:  $T = 2.0$

Variable	$f^{(1)}$	$f^{(1)}$	$f^{(1)}$	$f^{(1)}$
Grid	$t/T = 0.5$	$t/T = 1.0$	$t/T = 1.5$	$t/T = 2.0$
$40^2$	0.0124045	0.0199619	0.0271378	0.0363551
$80^2$	0.0072672	0.0108034	0.0151917	0.0176330
$160^2$	0.0038472	0.0064083	0.0087170	0.0101647

Variable	$f^{(2)}$	$f^{(2)}$	$f^{(2)}$	$f^{(2)}$
Grid	$t/T = 0.5$	$t/T = 1.0$	$t/T = 1.5$	$t/T = 2.0$
$40^2$	0.0325662	0.0380704	0.0529912	0.0523691
$80^2$	0.0206954	0.0167531	0.0267083	0.0263497
$160^2$	0.0092499	0.0070171	0.0112710	0.0107584

a perfect  $\gamma = 1.4$  gas. Both materials are at rest, initially, in a tube of length 1 m and separated by an impenetrable membrane at  $x = 0.7$  m. The analytical solution for this problem can be found. It consists of a left-moving rarefaction wave moving into the water, and a right-moving shock wave in the air. Our numerical solution after 230 ms is displayed in Fig. 10, obtained with a version of our algorithm, downgraded to Cartesian coordinates. The exact solution (dotted lines) is shown for comparison. The grid consists of 800 cells. Note that pressure oscillations near the water–air interface are absent, which was mentioned by [26,27] as the most difficult problem for the design of multi-phase Godunov methods. The pressure and density plotted here are volume-fraction-weighted averages when in a multi-material cell (there are no more than two such cells

VOF INTERFACE RECONSTRUCTION T= 3.75000E-01 CYCLE 120

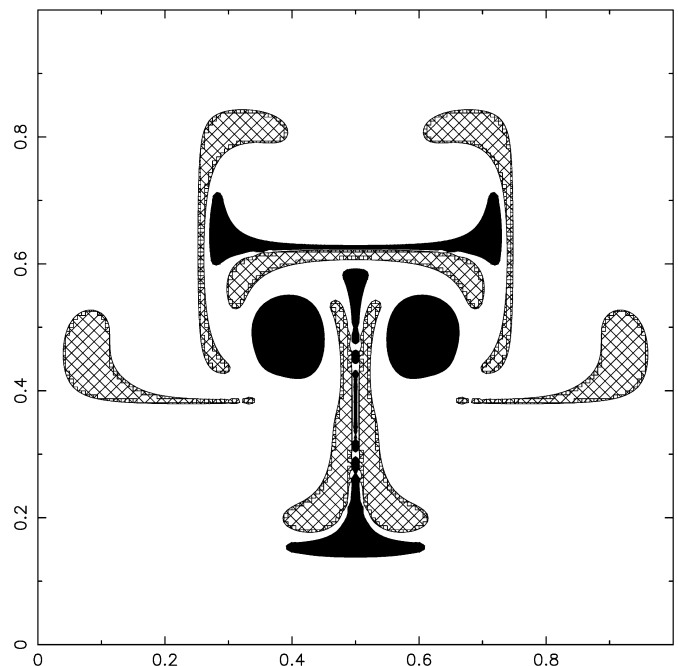


Fig. 8. Pure advection test with three materials in deformation velocity field with period  $T = 1.5$ , situation at moment of largest distortion  $t = T/4$ . Resolution:  $160^2$ . Initial state as in Fig. 6.

VOF INTERFACE RECONSTRUCTION T= 3.00000E+00 CYCLE 960

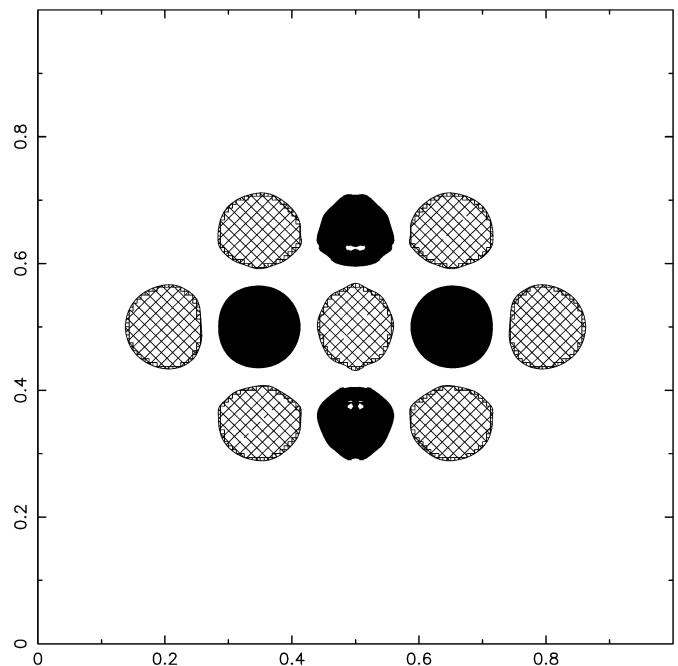


Fig. 9. Pure advection test with three materials in deformation velocity field with period  $T = 1.5$ , situation after two periods  $t = 2T$ . Resolution:  $160^2$ .

in the diagrams). In general, the solution is as close to physical reality as in the method by [26,28–30]. In particular, the contact discontinuity between materials is not diffuse in contrast to the schemes by [26,28–30] and the jump in density at the material interface occurs in only one cell. All wave propagation speeds

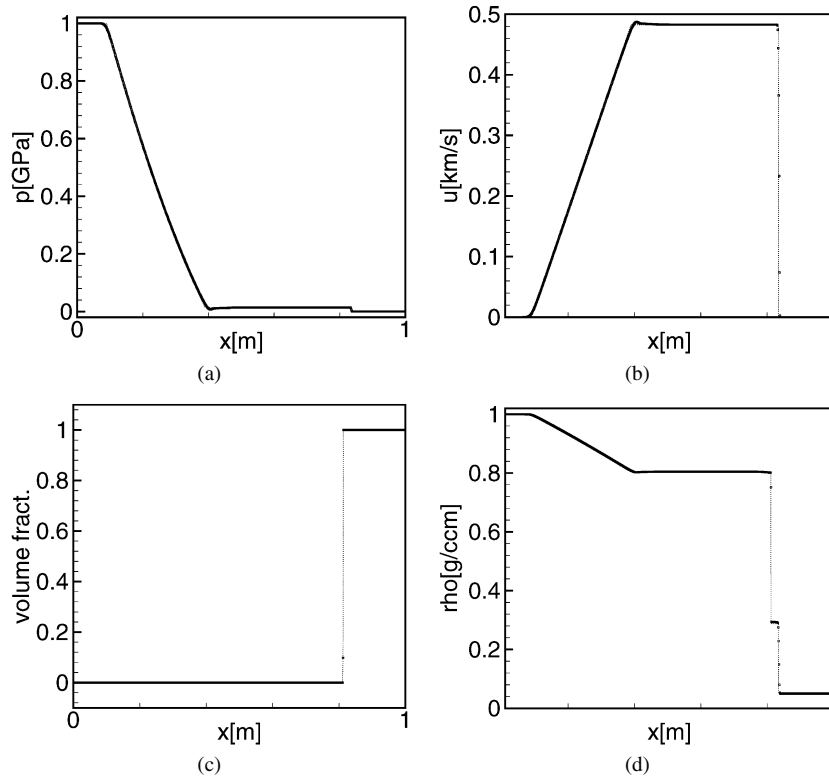


Fig. 10. (a) Pressure, (b) velocity, (c) air volume fraction, (d) density, for the water–air shock tube problem at  $t = 230$  ms. Exact solution shown as dotted line.

Table 5  
 $L_1$ -norm error for density  $\rho$  vs. resolution, water–air shock tube problem

Limiter	$\Delta x = 0.005$	$\Delta x = 0.0025$	$\Delta x = 0.00125$
minmod	0.00669867	0.00382602	0.00184427
mon. centred	0.00669598	0.00370905	0.00167813
van Leer	0.00670057	0.00374455	0.00171772
superbee	0.00668744	0.00363999	0.00161337

are accurately approximated by our scheme. Because of the large pressure ratio of 4 orders of magnitude the value of the pressure in the intermediate part is barely discernible. The part of the solution in the rarefaction fan is correctly approximated by the present scheme. Note a slight overshoot of velocity near the head of the rarefaction fan that is present in the numerical solutions by [26,28–30] as well. This phenomenon is accompanied by a minor undershoot of pressure at the same position. Table 5 lists the  $L_1$ -norm error of density for varying grid step  $\Delta x$ , the last column corresponding to the resolution in Fig. 10. Comparing the results for various slope limiters, the superbee limiter performs best. The only significant difference to the cases with the other three limiters is the error of the density of shocked air (lowest with superbee). The solution displayed in Fig. 10 is that obtained with the superbee limiter.

### 5.3. Planar impact of copper on ice

The next numerical example is more complicated and was stimulated by NASA's Deep Impact mission to the comet Tempel 1 in 2005. A copper plate of 2 m thickness strikes a target

of  $\text{H}_2\text{O}$  ice at a speed of  $10 \text{ km s}^{-1}$ . An extremely low-density ideal gas (adiabatic exponent  $\gamma = 1.4$ ) representing the coma fills the space behind the impactor-sample combination. The initial value of pressure is  $10^{-8} \text{ Pa}$  everywhere, and the gas density is  $10^{-9} \text{ g cm}^{-3}$  to simulate a situation close to vacuum in the coma outside the impactor-sample space. Normal densities of copper and ice are  $8.9$  and  $0.917 \text{ g cm}^{-3}$ , respectively. To avoid the formation of a vacuum, the gas in the wake behind the impactor is moving at  $10 \text{ km s}^{-1}$ . Tillotson's EOS [19], is used for both the metal and water ice. Parameters for low-temperature ice are due to [18].

This is an example with a highly non-linear EOS, an extreme density ratio at the contact discontinuity to the atmosphere at the rear of the impactor presents another difficulty. The computational domain has a length of 5 m. The impactor-sample interface is located at a coordinate of  $x = 2.5 \text{ m}$ , initially, and we use an equidistant mesh with 200 cells. Fig. 11 (a)–(d) shows total pressure, velocity, volume fraction and mass density resulting after a time of 150 ms. The density in Fig. 11(d) is the total value, the pressure displayed in Fig. 11(a) is the bulk pressure. For comparison, the exact solution, evaluated with the help of a semi-analytical method, the so-called “planar impact approximation” [23], is shown as dotted line. Two shock waves form, one is traveling backwards into the copper projectile, in a frame co-moving with the impactor, and the second propagates through the ice target. All propagation speeds, including that of the contact discontinuity are correctly approximated by the present scheme. Generally speaking, the agreement with theory is excellent. To investigate convergence we performed resolution enhancement and compared to the exact solution as in the

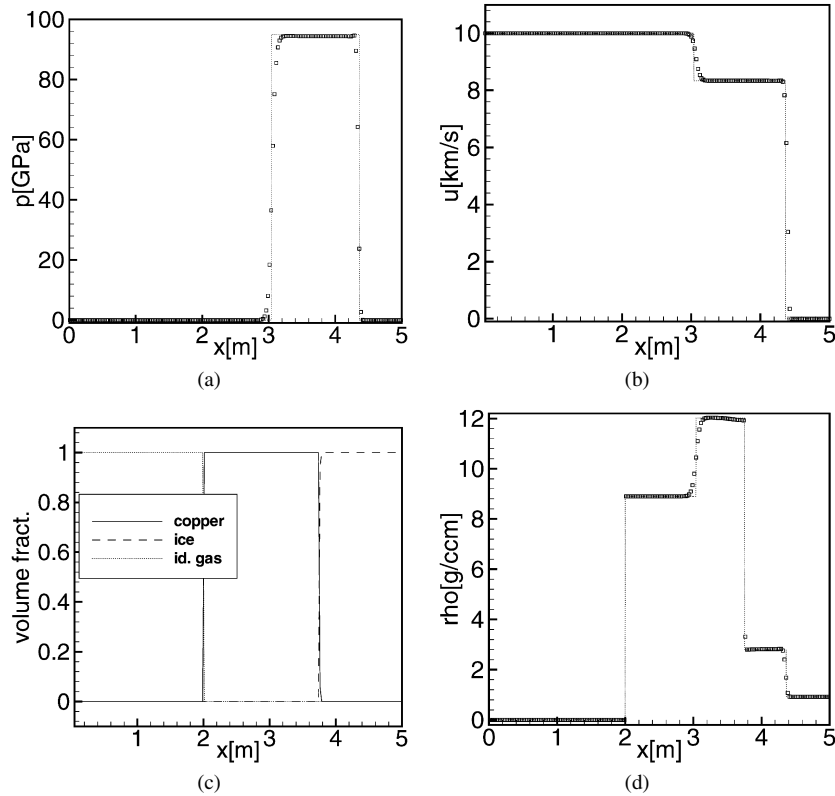


Fig. 11. (a) Total pressure, (b) velocity, (c) volume fraction, (d) mass density, 150 ms after impact of copper plate onto ice at  $10 \text{ km s}^{-1}$ . Projectile-target interface at 2.5 m, initially. Exact solution shown as dotted line.

Table 6  
 $L_1$ -norm error for density  $\rho$  vs. resolution, planar impact problem

Limiter	$\Delta x = 0.025$	$\Delta x = 0.0125$	$\Delta x = 0.00625$
minmod	0.00837377	0.00476984	0.00346751
mon. centred	0.00808121	0.00420641	0.00258596
van Leer	0.00809010	0.00432188	0.00280961
superbee	0.00819433	0.00445247	0.00284260

previous example. Results are given in Table 6. Because the domain is not of unit length the  $L_1$  norm error is scaled by a factor of 1/5 to be able to compare to the previous example. Here the best variant is that with the monotized centred limiter although the difference to superbee is not large. Fig. 11 displays the superbee case.

#### 5.4. Asteroid impact into an ocean

Our two-dimensional axisymmetric numerical example in an external gravity field is devoted to a geophysically important question: the fate of a large cosmic body during an impact into the deep ocean of the earth. This is a more probable scenario than meteorite impact into shallow sea or onto the continents, although direct evidence in the form of a crater is rare. The axisymmetric formulation allows to study the main aspects of this problem at high resolution. High-velocity impact craters on the moon and the terrestrial planets are axially symmetric to a good degree of approximation although the most probable angle of incidence is 45 degrees [23]. Several authors studied various

questions related to marine impact such as the amount of shock-induced modifications in the oceanic crust (Artem'eva and Shuvalov, 2002 [21]), the conditions of the formation of a crater on the ground [22], depending on the impactor-diameter-to-ocean-depth ratio. Other phenomena studied are the complexities of the late stage excavation flow in comparison with laboratory experiments, such as the appearance of jets and surges, and the generation of tsunami (see Gisler et al. (2003) [20]). The fate of to the impacting body was less relevant in most previous studies. In other cases, the impactor has been assumed to consist of the same material as the oceanic crust [21], for simplicity. So meteorite material was indistinguishable from crustal ejecta and the question if large amounts of meteorite material may leave the ocean after a transient phase of a growing steam-filled cavity remains unanswered. It is also interesting to know the velocity of impactor material when it leaves the cavity to estimate the ballistic range of such ejecta. The answer partially depends on the composition of the impacting body that may be a stony or iron asteroid, or a comet. Tillotson's EOS is used for the oceanic water and the impactor made of granite, both with EOS parameters from [23]. The third material is air taken as an ideal gas with adiabatic exponent 1.4. The impact speed is  $20 \text{ km s}^{-1}$ , and the impactor has a diameter of 1 km, it is situated on top of the water surface, initially. Because we do not study submarine crater formation (this would require a fourth material), we let the asteroid impact into an ocean of 5.5 km depth, with a reflective boundary condition at the bottom. The initial state of the atmosphere and the ocean is one of hydrostatic equilibrium

in a constant gravitational field  $g_z = -9.81 \text{ m s}^{-2}$ , satisfying the discrete Euler equation exactly. The ocean initially has a constant internal energy that would correspond to a pressure of one atmosphere at the normal density  $\rho_0 = 0.998 \text{ g cm}^{-3}$ . The pressure at the air–water interface is exactly one atmosphere, to guarantee this, the cell-centred values of the density above and below the water surface are determined from the condition of acceleration matching, see [13].

The computational domain has a width of 20 km in both the radial and vertical directions, the resolution of the equidistant mesh is 800 by 800 cells, there are 40 cells per projectile diameter, sufficient to study melting and evaporation [24]. The left boundary is the symmetry axis (in figures we mirror data at the symmetry axis), whereas at the right and top boundaries, non-reflecting boundary conditions are imposed. We took extra care of constructing a correct discrete version of hydrostatic equilibrium compatible with the discretization on a staggered mesh, by solving the non-linear Euler equation (time derivative of velocity equal to zero) to obtain cell-centred values of the density in the  $z$ -direction. Hydrostatic layering of pressure is still present in the region undisturbed by the flow (see Figs. 12 and 13, respectively). Logarithmically spaced contours of pressure are shown in Figs. 12, 13 corresponding to 0.08 and 2.8 s after the impact, respectively. The maximum pressure after 0.08 s is around  $\sim 145 \text{ GPa}$  (the peak pressure in the impactor is even higher, at earlier times), but it has already decayed by two orders of magnitude after 2.8 s. A system of shocks and rarefaction waves in the water and the air has developed. The shock wave is partially reflected from the bottom, see Fig. 13. The shape of the water cavity and the form of the outer rim can be recognized in the pressure contours. Moreover a complicated structure of atmospheric flow outward of the contact discontinuity to the air can be seen in Fig. 13. Despite the method uses artificial viscosity, shocks are spread over few zones, only. The maximum pressure in Fig. 12 is sufficient to melt rocks but too low for complete evaporation, see [24]. Fig. 14 shows color-coded density distributions of water and the impactor material

at a time of 16 s after the impact. Only part of the computational mesh is displayed in the radial direction. Although 16 s are already quite a long time as compared to the scale of penetration  $D/v = 0.05 \text{ s}$ , where  $D$  is the asteroid diameter, the transient cavity is still growing (see Gisler et al., 2003 [20]). Its outer rim above the water surface is a material boundary to the air. Dense water vapor dominates inside the cavity. The impactor evolves through Raleigh–Taylor and Kelvin–Helmholtz instabilities [20,21]. Therefore it has a complicated fractal shape, nevertheless it also contains coherent parts. Note, that there are mixed cells where both water and meteorite debris are present. Density values of meteorite debris are comparable to the density of steam in such mixed cells. Due to limitations of the

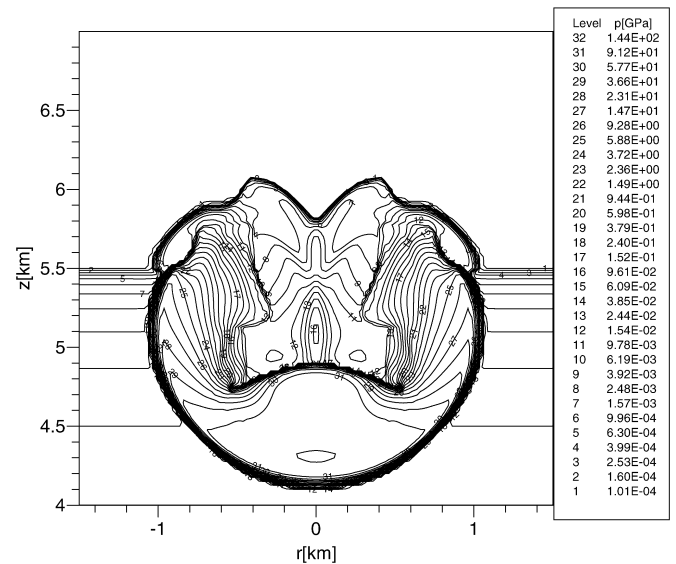


Fig. 12. Pressure contours, 0.08 s after the impact of a 1 km diameter stony asteroid; zoomed part of entire computational domain (ca. 30 cells in  $r$  and 60 in  $z$ -directions). Contours are equidistant in  $\log p$ , from 144 GPa down to  $1.01325 \times 10^{-4} \text{ GPa}$  (one atmosphere). Only part of the computational domain shown.

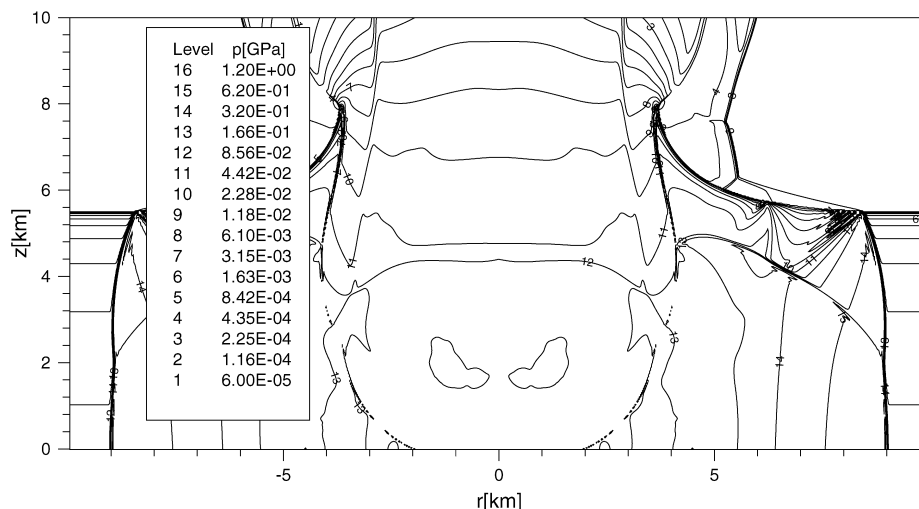


Fig. 13. Pressure contours, 2.8 s after impact of a 1 km diameter stony asteroid. Contours are equidistant in  $\log p$ , from 1.2 GPa down to  $6 \times 10^{-5} \text{ GPa}$ . Note hydrostatic layering in the outer part not yet reached by shocks. Undisturbed surface at  $z = 5.5 \text{ km}$ . Only part of the computational domain shown.



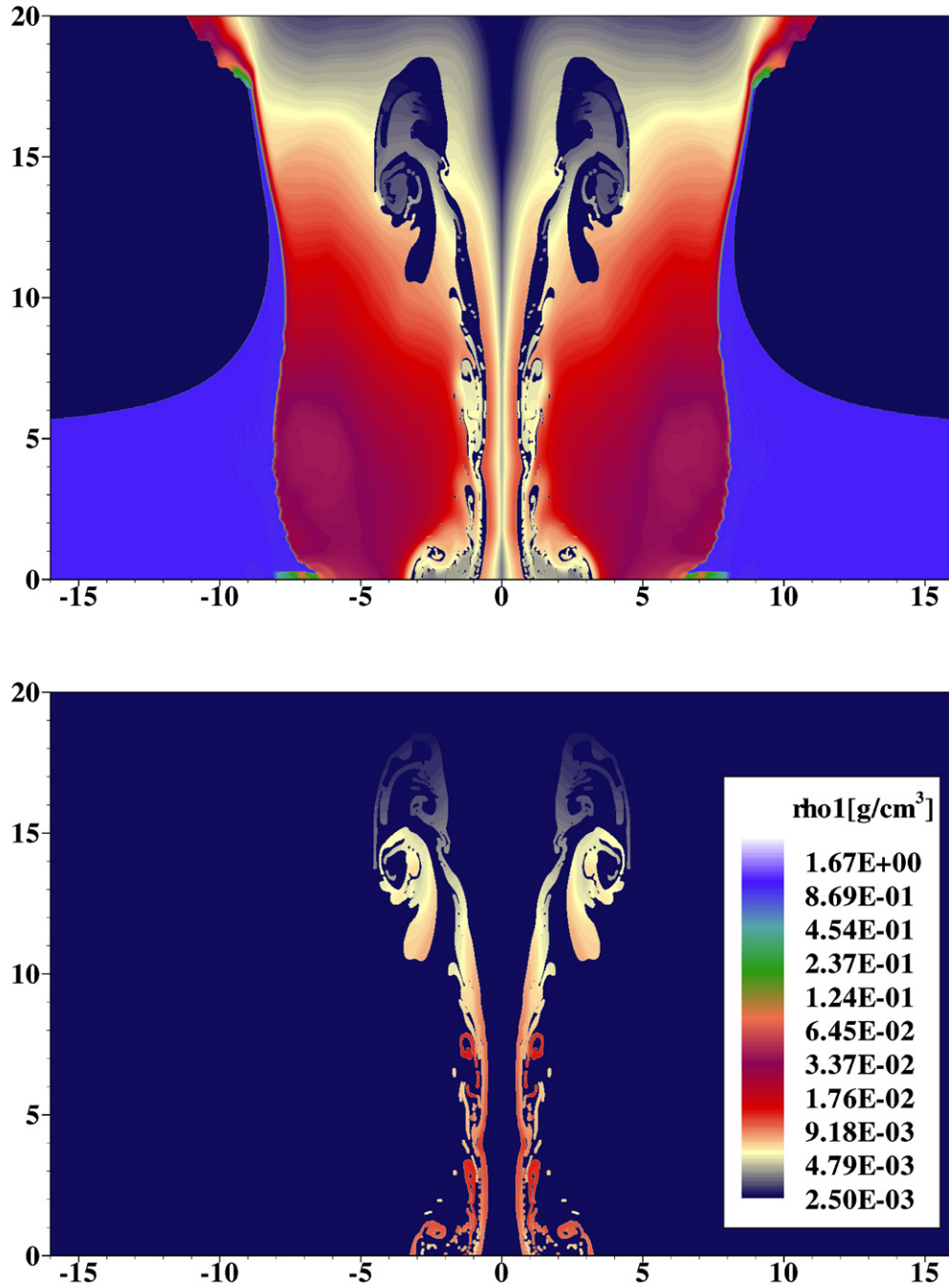


Fig. 14. Upper panel: Density of oceanic water, 16 s after the impact. Lower panel: Density of asteroid material, 16 s after the impact. Note: Dark blue corresponds to other materials not shown here. Material interface not drawn. Only part of the computational domain shown.

of the water surface, initially. Because we do not study submarine crater formation (this would require a fourth material), we let the asteroid impact into an ocean of 5.5 km depth, with a reflective boundary condition at the bottom. The initial state of the atmosphere and the ocean is one of hydrostatic equilibrium in a constant gravitational field  $g_z = -9.81 \text{ m s}^{-2}$ , satisfying the discrete Euler equation exactly. The ocean initially has a constant internal energy that would correspond to a pressure of one atmosphere at the normal density  $\rho_0 = 0.998 \text{ g cm}^{-3}$ . The pressure at the air–water interface is exactly one atmosphere, to guarantee this, the cell-centred values of the density above and

below the water surface and determined from the condition of acceleration matching, see [13].

The computational domain has a width of 20 km in both the radial and vertical directions, the resolution of the equidistant mesh is 800 by 800 cells, there are 40 cells per projectile diameter, sufficient to study melting and evaporation [24]. The left boundary is the symmetry axis (in figures we mirror data at the symmetry axis), whereas at the right and top boundaries, non-reflecting boundary conditions are imposed. We took extra care of constructing a correct discrete version of hydrostatic equilibrium compatible with the discretization on a staggered

mesh, by solving the non-linear Euler equation (time derivative of velocity equal to zero) to obtain cell-center values of the density in the  $z$ -direction. Hydrostatic layering of pressure is still present in the region undisturbed by the flow (see Figs. 12 and 13, respectively). Logarithmically spaced contours of pressure are shown in Figs. 12, 13 corresponding to 0.08 and 2.8 s after the impact, respectively. The maximum pressure after 0.08 s is around  $\sim 145$  GPa (the peak pressure in the impactor is even higher, at earlier times), but it has already decayed by two orders of magnitude after 2.8 s. A system of shocks and rarefaction waves in the water and the air has developed. The shock wave is partially reflected from the bottom, see Fig. 13. The shape of the water cavity and the form of the outer rim can be recognized in the pressure contours. Moreover a complicated structure of atmospheric flow outward of the contact discontinuity to the air can be seen in Fig. 13. Despite the method uses artificial viscosity, shocks are spread over few zones, only. The maximum pressure in Fig. 12 is sufficient to melt rocks but too low for complete evaporation, see [24]. Fig. 14 shows color-coded density distributions of water and the impactor material at a time of 16 s after the impact. Only part of the computational mesh is displayed in the radial direction. Although 16 s are already quite a long time as compared to the scale of penetration  $D/v = 0.05$  s, where  $D$  is the asteroid diameter, the transient cavity is still growing (see Gisler et al., 2003 [20]). Its outer rim above the water surface is a material boundary to the air. Dense water vapor dominates inside the cavity. The impactor evolves through Raleigh–Taylor and Kelvin–Helmholtz instabilities [20,21]. Therefore it has a complicated fractal shape, nevertheless it also contains coherent parts. Note, that there are mixed cells where both water and meteorite debris are present. Density values of meteorite debris are comparable to the density of steam in such mixed cells. Due to limitations of the commercial graphics rendering software, the density is always drawn as color-coded value when the material is present without respecting the material interface; colors should only be displayed in the part of the computational cell where the particular material is. Parts of asteroid debris have reached an altitude of 10 km above the water surface, from a location near the ground. A few percent in mass of the impactor left the computational domain earlier through the upper boundary. The time scale of this motion is indicative of a velocity of  $\sim 1\text{--}1.25$  km s $^{-1}$ . The simulations shown in this work have been carried out on a single-processor desktop PC; the asteroid impact example took less than a day of CPU time.

## 6. Concluding remarks

We presented a new Eulerian multi-material hydrodynamics algorithm that is able to compute flows with strong shock waves in axial symmetry. Various aspects of our method like the implementation of VOF interface tracking in cylindrical coordinates, the advection of momentum on a staggered mesh, compatible discretization in the sense of [31], and the approach for the advective mass flux of individual materials are not restricted to the special type of the algorithm. The emphasis was

on a very robust method, able to cope with rather general EOS and with source terms arising from external forces. Where other authors preferred to use VOF interface tracking and the discretization of the evolution equation for material volume in a less comprehensive manner, we have achieved an entirely algebraic formulation. A generalization to cylinder coordinates was achieved using transformation properties of a radial centroid coordinate for each material. The additional effort compared to Cartesian coordinates is relatively low. Our material volume advection scheme avoids unnecessary calculations by computing only quantities that are nonzero for multi-material edges. The resulting algorithm is completely volume-filling and overshoot-free, in contrast to other formulations like [7]. A construction of onion skin ordering in the case of three materials is described in this work. It takes special care to maintain interface line directions consistent with a gradient approximation of volume fraction and to avoid multiple trials to reconstruct interfaces for material groups. The advective flux of mass (and internal energy) is constructed by characteristic traceback evaluating mass contained in the domain of dependence for each material separately. This region is determined with the help of spatially linear interpolation of velocity during the Lagrangian step.

The one-dimensional numerical examples show that the method correctly approximates solutions for strong shocks and rarefaction waves involving very different materials and highly non-linear EOS. In particular no oscillations of pressure or velocity at contact discontinuities between materials result. Examples of pure advection in two dimensions for the VOF method with three materials in incompressible velocity fields are given as well. The two-dimensional axisymmetric impact example demonstrates the ability to solve complex flow problems in an external gravity field where late-time dynamics of the cavity is gravity-dominated, see [23]. The particular type of the algorithm enables us to include more complicated physics in the future. Generalization to three-dimensional Cartesian coordinates is straightforward but requires more computing resources than a desktop computer.

## Appendix A. Compatible discretization in the radial direction

Because of the use of a staggered grid evolution equations for momentum and cell-centred quantities like density and internal energy are defined with respect to different, but overlapping grids. A compatible discretization in the sense of [31] has the property that the change of total energy is described in a conservative way. This justifies our somewhat ad hoc introduction of the terms for the discrete divergence of velocity and the particular form of the discrete Euler equation. We only discuss the radial direction, the derivation for the vertical direction is similar. The Lagrangian step conserves mass. Therefore the change of kinetic energy associated with the node  $i$  during the Lagrangian step can be found by multiplying the discrete Euler equation, Eq. (13), with  $M_i$  and the time-averaged velocity  $u_i^* = (\tilde{u}_i + u_i)/2$

$$M_i(\tilde{u}_i - u_i)\frac{1}{2}(\tilde{u}_i + u_i) = r_i(p_{i-1/2}^{n+1/2} - p_{i+1/2}^{n+1/2})u_i^* \Delta t. \quad (\text{A.1})$$

Note, that the last equation follows from the discrete Euler equation only because of the very special construction of the nodal mass  $M_i$ . Recall that the definition of the nodal masses  $M_i$ , Eq. (36) has an interpretation as weighted average of adjacent cell masses, although it is not based on a control volume. The second component of velocity does not change during the step in the radial direction, so it disappears here. A definition of internal energy associated with edge  $i$  of the staggered mesh, consistent with the mass average Eq. (36), is

$$M_i \epsilon_i := \frac{1}{2}[(1 + \zeta_{i-1/2})M_{i-1/2}\epsilon_{i-1/2} + (1 - \zeta_{i+1/2})M_{i+1/2}\epsilon_{i+1/2}], \quad (\text{A.2})$$

where  $\epsilon_{i+1/2}$  is the following mass-fraction weighted average over materials

$$\rho_{i+1/2}\epsilon_{i+1/2} := \sum_m f_{i+1/2}^m \rho_{i+1/2}^m \epsilon_{i+1/2}^m. \quad (\text{A.3})$$

With the help of (22), (A.2), and after a little algebra, one finds the change of the internal energy associated with node  $i$ :

$$M_i(\tilde{\epsilon}_i - \epsilon_i) = -\frac{\Delta t}{2}[(1 + \zeta_{i-1/2})p_{i-1/2}^{n+1/2}(r_i u_i^* - r_{i-1} u_{i-1}^*) + (1 - \zeta_{i+1/2})p_{i+1/2}^{n+1/2}(r_{i+1} u_{i+1}^* - r_i u_i^*)]. \quad (\text{A.4})$$

After some rearrangement the total energy difference can be written as

$$\begin{aligned} \tilde{E}_i^{(\text{tot})} - E_i^{(\text{tot})} &= M_i \left( \frac{\tilde{u}_i^2}{2} + \tilde{\epsilon}_i - \frac{u_i^2}{2} - \epsilon_i \right) \\ &= \frac{1}{2}[r_{i-1} u_{i-1}^* (1 + \zeta_{i-1/2}) + r_i u_i^* (1 - \zeta_{i-1/2})] p_{i-1/2}^{n+1/2} \Delta t \\ &\quad - \frac{1}{2}[r_i u_i^* (1 + \zeta_{i+1/2}) + r_{i+1} u_{i+1}^* (1 - \zeta_{i+1/2})] p_{i+1/2}^{n+1/2} \Delta t. \end{aligned} \quad (\text{A.5})$$

Eq. (A.5) is in flux-difference form, thus total energy is conserved. The acceleration due to an external force was set to zero; such a force will do non-conservative work in general. Where [31] regarded conservation of total energy in a cell-centred fashion demanding to split kinetic energy from two adjacent nodes, we preferred to introduce quantities like  $\epsilon_i$  referred to the nodes  $i$  and to regard conservation with respect to the dual grid used for momentum.

## References

- [1] D.J. Benson, Computational methods in Lagrangian and Eulerian hydrocodes, *Comput. Meth. Appl. Mech. Eng.* 99 (1992) 235.
- [2] W.J. Rider, D.B. Kothe, Reconstructing volume tracking, *J. Comput. Phys.* 141 (1998) 112.
- [3] D. Gueyffier, J. Li, R. Scardovelli, S. Zaleski, Volume-of-fluid interface tracking with smoothed surface stress methods for three-dimensional flow, *J. Comput. Phys.* 152 (1999) 423.
- [4] J.E. Pilliod Jr., E.G. Puckett, Second-order accurate volume-of-fluid algorithms for tracking material interfaces, *J. Comput. Phys.* 199 (2004) 465.
- [5] D.J. Benson, Volume of fluid interface reconstruction methods for multi-material problems, *Appl. Mech. Rev.* 55 (2) (2002) 151.
- [6] S. Osher, J.A. Sethian, Fronts propagating with curvature-dependent speed: Algorithms based on Hamilton–Jacobi formulations, *J. Comput. Phys.* 79 (1988) 12.
- [7] G.H. Miller, E.G. Puckett, A high-order Godunov method for multiple condensed phases, *J. Comput. Phys.* 128 (1996) 134.
- [8] G.H. Miller, P. Colella, A conservative three-dimensional Eulerian method for coupled solid–fluid shock capturing, *J. Comput. Phys.* 183 (2002) 26.
- [9] R.J. LeVeque, Balancing source terms and flux gradients in high-resolution Godunov methods: the quasi-steady wave-propagation algorithm, *J. Comput. Phys.* 146 (1998) 446.
- [10] J.M. McGlaun, S.L. Thompson, M.G. Elrick, CTH: A three-dimensional shock wave physics code, *Int. J. Impact Eng.* 10 (1990) 351.
- [11] V.V. Shuvalov, Multimaterial hydrodynamic code SOVA for interfacial flows, application to thermal layer effect, *Shock Waves* 9 (1999) 381.
- [12] V.V. Shuvalov, N.A. Artem'eva, I.B. Kosarev, 3D Hydrodynamic code SOVA for multimaterial flows, application to Shoemaker–Levy 9 comet impact problems, *Int. J. Impact Eng.* 23 (1999) 847.
- [13] E.S. Oran, J.P. Boris, *Numerical Simulation of Reactive Flow*, Elsevier, New York, 1987.
- [14] M. Holt, *Numerical Methods in Fluid Dynamics*, Springer, Berlin, Heidelberg, New York, Tokyo, 1984.
- [15] E. Aulisa, S. Manservigi, R. Scardovelli, S. Zaleski, A geometrical area-preserving volume-of-fluid advection method, *J. Comput. Phys.* 192 (2003) 355.
- [16] M. Baum, T. Poinso, D. Thevenin, Accurate boundary conditions for multicomponent reactive flows, *J. Comput. Phys.* 116 (1994) 247.
- [17] D.J. Benson, Eulerian finite element methods for the micromechanics of heterogeneous materials: Dynamic prioritization of material interfaces, *Comput. Meth. Appl. Mech. Eng.* 151 (1998) 343.
- [18] W. Benz, E. Asphaug, Catastrophic disruptions revisited, *Icarus* 142 (1999) 5.
- [19] J.H. Tillotson, Metallic equations of state for hypervelocity impacts, *General Atomic Report GA-3216*, 1962.
- [20] G. Gisler, R. Weaver, Ch. Mader, M. Gittings, Two- and three-dimensional simulations of asteroid ocean impacts, *Science of Tsunami Hazards* 21 (2) (2003) 119.
- [21] N.A. Artem'eva, V.V. Shuvalov, Shock metamorphism on the ocean floor (numerical simulations), *Deep Sea Res. Pt. II: Topical Studies in Oceanography* 49 (6) (2002) 959.
- [22] M. Lindström, V. Shuvalov, B. Ivanov, Lockne crater as a result of marine-target oblique impact, *Planet. Space Sci.* 53 (2005) 803.
- [23] H.J. Melosh, *Impact Cratering: A Geologic Process*, Oxford University Press/Clarendon Press, New York/Oxford, 1989.
- [24] E. Pierazzo, A.M. Vickery, H.J. Melosh, A reevaluation of impact melt production, *Icarus* 127 (1997) 408.
- [25] A.K. Kapila, R. Menikoff, J.B. Bdzil, S.F. Son, D.S. Stewart, Two-phase modeling of deflagration-to-detonation transition in granular materials: Reduced equations, *Phys. Fluids* 13 (10) (2001) 3002.
- [26] R. Saurel, R. Abgrall, A Godunov method for compressible multifluid and multiphase flow, *J. Comput. Phys.* 150 (1999) 425.
- [27] R. Abgrall, S. Karni, Computations of compressible multifluids, *J. Comput. Phys.* 169 (2001) 594.
- [28] R. Saurel, O. LeMetayer, A multiphase model for compressible flows with interfaces, shocks, detonation waves and cavitation, *J. Fluid. Mech.* 431 (2001) 239.
- [29] A. Chinnayya, E. Daniel, R. Saurel, Modelling detonation waves in heterogeneous energetic materials, *J. Comput. Phys.* 196 (2004) 490.
- [30] A. Murrone, A. Guillard, A five equation reduced model for compressible two phase flow problems, *J. Comput. Phys.* 202 (2005) 664.
- [31] E.J. Caramana, D.E. Burton, M.J. Shashkov, P.P. Whalen, The construction of compatible hydrodynamic algorithms utilizing conservation of total energy, *J. Comput. Phys.* 146 (1998) 227.